



Filtered Density Function Simulations of a Near-Limit Turbulent Lean Premixed Flame

Hua Zhou* and Zhuyin Ren†

Tsinghua University, 100084 Beijing, People's Republic of China

David H. Rowinski‡

Convergent Science, Inc., Madison, Wisconsin 53719

and

Stephen B. Pope§

Cornell University, Ithaca, New York 14853

<https://doi.org/10.2514/1.B37707>

The predictive numerical simulation of near-limit turbulent premixed combustion, in which the turbulent intensity is high and the fuel/air mixture is near the flammability limit, remains challenging. In this study, large-eddy simulation (LES)/filtered density function (FDF) simulations of a high-speed piloted premixed jet burner flame are performed to illustrate the importance of the resolved level of reactive scalars and micromixing modeling on predicting the overall combustion process. The simulations with increased resolved levels of reactive scalars yield notably improved predictions throughout the extinction–reignition region of this flame. The sources of grid sensitivity are thoroughly examined through the quantification of the resolved levels of the velocity and scalar fields, as well as the mixing–reaction budgets. Subgrid mixing is identified as the most prominent factor for grid sensitivity. The effects of mixing timescale modeling are investigated and quantified through a parametric study of the mixing rate parameter and the development of an augmented hybrid mixing timescale model in the LES context. As far as the mixing formulation is concerned, the Euclidean minimum spanning tree model shows a lower level of grid dependence than the interaction by exchange with the mean model due to the enforcement of localness in composition space.

Nomenclature

C_M	=	mixing rate parameter
l_η	=	Kolmogorov length scale, m
S_i	=	reaction rate of composition i , 1/s
\tilde{U}	=	density-weighted spatially filtered velocity, m/s
\mathbf{x}	=	physical location, m
Y_i	=	mass fraction of composition i
$\tilde{\Gamma}_i$	=	density-weighted spatially filtered molecular diffusivity of composition i , m^2/s
$\tilde{\Gamma}_t$	=	density-weighted spatially filtered turbulent diffusivity, m^2/s
Δ	=	filter width, m
$\tilde{\rho}$	=	spatially filtered density, kg/m^3
ϕ_i	=	specific mole number of composition i , mole/kg
Ω_f	=	flame-induced subgrid mixing frequency, 1/s
Ω_M	=	mixing frequency, 1/s
Ω_t	=	subgrid turbulence frequency, 1/s

I. Introduction

TURBULENT lean premixed combustion is one of the promising techniques to meet the ever increasingly stringent emission regulations for both aeroengines and industrial gas turbines [1]. By operating combustors under the lean premixed conditions, the local

equivalence ratio maintains at a low level so that the local hot spots get eliminated, minimizing the production of thermal nitrogen oxides (NO_x), and thus the overall NO_x emission [2]. An inherent problem to lean premixed combustors is related to engine turndown ratio. Namely, for a combustor designed to operate with a low equivalence ratio under a high load, it needs to operate with a very lean mixture near the flammability limit at the low-power level. Moreover, combustors of this type usually feature high turbulent intensity to accomplish a high level of premixing [3], resulting in intense turbulence–chemistry interaction, which further causes complex near-limit combustion phenomena, e.g., local extinction/reignition and trigger flame instability. These could eventually lead to blowout or intense thermal-acoustic instability, bringing structural damages to engines [4,5]. Therefore, it is essential, although challenging, for combustion simulation to capture these near-limit flame phenomena for reliable engine design.

A set of piloted premixed jet burner (PPJB) flames have been developed for investigating turbulence–chemistry interactions in lean and highly turbulent premixed flames [6,7]. This configuration is attractive in the sense that it has a simplified geometry while featuring the key combustion characteristics of our interest, i.e., a very high turbulence intensity and a near-lean-flammability-limit equivalence ratio. More important, detailed measurements on temperature and species allow systematic comparison with model predictions. The burner consists of a high-speed lean premixed (equivalence ratio 0.5) methane–air central jet with a jet diameter of $D = 4$ mm and a low-speed hot pilot composed of stoichiometric methane–air burned products, and it is surrounded by a coflow of lean premixed hydrogen–air burned products. The PM1 flame series consists of four flames denoted as PM1-50, PM1-100, PM1-150, and PM1-200 corresponding to the central jet bulk velocities of 50, 100, 150, and 200 m/s, respectively. The turbulence–chemistry interaction becomes stronger with the increase of the central jet velocity as indicated by the flame luminosity. The PM1-150 flame exhibits reduced luminosity between the axial location x/D of 15.0 and 30.0, followed by a prominent increase of luminosity. Meanwhile, the PM1-200 flame is close to global extinction.

A variety of turbulent combustion models have demonstrated their success for the low-speed flames of PM1-50 and PM1-100 [8–11]. However, the high-speed flames of PM1-150 and PM1-200 remain challenging, despite substantial computational efforts that have

Received 14 June 2019; revision received 1 December 2019; accepted for publication 6 December 2019; published online 27 January 2020. Copyright © 2019 by the American Institute of Aeronautics and Astronautics, Inc. All rights reserved. All requests for copying and permission to reprint should be submitted to CCC at www.copyright.com; employ the eISSN 1533-3876 to initiate your request. See also AIAA Rights and Permissions www.aiaa.org/randp.

*Research Assistant, Center for Combustion Energy; huazhou_2018@163.com.

†Professor, Center for Combustion Energy and Institute for Aerospace Engineering; zhuyinren@tsinghua.edu.cn. Senior Member AIAA (Corresponding Author).

‡Applications Engineer; [dhr3b1@gmail.com](mailto: dhr3b1@gmail.com).

§Professor, Sibley School of Mechanical and Aerospace Engineering; stephen.b.pope@gmail.com.

been made with various modeling approaches [10–13]. For flame PM1-150, although the predicted mean and root mean square (rms) properties of the mixture fraction match reasonably well with the experiment, the reaction progress is in general significantly over-predicted and the extinction–reignition process cannot be accurately reproduced. There have been several studies [10,12,13] on different aspects of modeling (e.g., chemical kinetics, micromixing models, and inlet boundaries) in order to understand the origin of the modeling inaccuracy. None have been successful but, nevertheless, these works are of value in eliminating possible causes and making small improvements. Transported probability density function (TPDF) methods have shown some promise toward better prediction for these flames. The TPDF simulations in the Reynolds-averaged Navier–Stokes (RANS) context by Dunn et al. [12] show that the axial variation of the level of turbulence–chemistry interaction for flame PM1-150 gets qualitatively better predicted by increasing the mixing rate parameter from 1.0 to 8.0. In conjunction with the large-eddy simulation (LES), the LES/filtered density function (FDF) simulation by Rowinski and Pope [13] yielded reasonable predictions of the PM1-150 flame in terms of the species radial profiles up to $x/D = 30.0$, together with a systematic investigation of the effects of inlet boundary conditions, chemical kinetics, and the mixing rate parameter C_M on macroscopic flame characteristics. The study showed that good predictions up to x/D of 30.0 can be achieved by increasing C_M from 5.0 to 20.0. However, the overprediction of the combustion process was still severe at $x/D = 45.0$, and a further increase of C_M resulted in minor improvement. The underlying physics for the overpredicted combustion process is still unclear. Meanwhile, although a grid convergence study on the statistics of velocities and mixture fraction has been carried out in Ref. [13], the resolved level of reactive scalar fields has not been quantified. Moreover, the effects of grid resolution and micromixing modeling on subgrid physiochemical processes warrant further investigation.

In this work, LES/FDF simulations of the PM1-150 flame are performed, which yield notably improved predictions throughout the extinction–reignition region by increasing grid resolution. The effects of grid resolution are investigated from the perspective of the resolved level of the velocity and scalar fields. The profound effects of grid resolution on subgrid physiochemical processes are investigated via a mixing–reaction budget analysis. The effects of mixing timescale modeling on the predicted combustion process are investigated through a parametric study of the mixing rate parameter and the augmentation of a timescale model for reactive scalars. The importance of the mixing formulation is illustrated by comparing the predictions from the interaction by exchange with the mean (IEM) and Euclidean minimum spanning tree (EMST) models.

The rest of the paper is organized as follows. In Sec. II, the LES/FDF methodology and the simulation settings are presented. In Sec. III, the predicted time-averaged radial profiles are presented, followed by the flame structure analysis. In Sec. IV, the resolved level of velocity and reactive scalar fields is quantified, followed by the mixing–reaction budget analysis. In Sec. V, a parametric study of the mixing rate parameter C_M and the comparison between the IEM and EMST models are presented, followed by a discussion on a hybrid mixing timescale model. Conclusions are in Sec. VI.

II. LES/FDF Methodology and Simulation Settings

The LES/FDF approach employed is based on a two-way coupled hybrid scheme between a finite volume solver and a Monte Carlo particle solver [14–16]. The subgrid turbulence–chemistry interaction is resolved through the joint composition probability density function. Specifically, the finite volume solver solves the following modeled continuity and momentum transport equations:

$$\frac{\partial \bar{\rho}}{\partial t} + \nabla \cdot (\bar{\rho} \bar{\mathbf{U}}) = 0 \quad (1)$$

$$\begin{aligned} \frac{\partial \bar{\rho} \bar{\mathbf{U}}}{\partial t} + \nabla \cdot (\bar{\rho} \bar{\mathbf{U}} \bar{\mathbf{U}}) \\ = -\nabla \bar{p} + \nabla \cdot \left[\bar{\rho} (\bar{\mathbf{v}} + \bar{\mathbf{v}}_t) \left(\nabla \bar{\mathbf{U}} + (\nabla \bar{\mathbf{U}})^T - \frac{2}{3} I \nabla \cdot \bar{\mathbf{U}} \right) \right] \end{aligned} \quad (2)$$

where the bar (-) and the tilde ($\tilde{\cdot}$) denote spatial filtering and density-weighted spatial filtering, respectively. $\bar{\mathbf{U}}$, $\bar{\rho}$, and \bar{p} are the filtered velocity, density, and pressure, respectively. Also, $\bar{\mathbf{v}}$ and $\bar{\mathbf{v}}_t$ are the filtered molecular and subgrid turbulent viscosities. These equations are cast in a cylindrical coordinate, with a second-order conservative scheme being applied for discretization. More details about the solution algorithm can be found in Ref. [17]. Continuity is enforced through solving the pressure Poisson equation. Note that, as the filtered density computed from the computational particles contains considerable random noise due to the nature of the Monte Carlo approach, a transport equation for the specific volume (reciprocal of the filtered density, $1/\bar{\rho}$) is solved to obtain a smoothed filtered density consistent with the computational particles [16]. In the Monte Carlo particle solver, each computational particle carries the properties including composition ϕ , position \mathbf{x} , and mass m ; and the evolution of the particles in physical and composition space is governed by the following stochastic differential equations:

$$d\mathbf{x}^* = [\bar{\mathbf{U}} + \nabla(\bar{\Gamma} \bar{\rho})/\bar{\rho}]^* dt + (2\bar{\Gamma}_t^*)^{1/2} d\mathbf{W}^* \quad (3)$$

$$d\phi^*(t) = \mathbf{M}(\phi^*) dt + (\nabla \cdot (\bar{\rho} \bar{\Gamma} \nabla \phi^*)/\bar{\rho})^* dt + \mathbf{S}(\phi^*) dt \quad (4)$$

where $\bar{\Gamma}$ and $\bar{\Gamma}_t$ are the filtered molecular and turbulent diffusivities, $d\mathbf{W}^*$ is an independent Wiener increment, $\mathbf{S}(\phi^*)$ is the reaction rate, and $\mathbf{M}(\phi^*)$ represents the rate of change due to subgrid mixing. For the IEM model [18], $\mathbf{M}(\phi^*) = \Omega_M^* \times (\bar{\phi}^* - \phi^*)$, where Ω_M^* represents the mixing frequency. The superscript * denotes either an individual particle property or a value of the filtered LES field evaluated at the particle's location. According to Eq. (4), the effects of molecular diffusion are treated by the first two terms on the right-hand side. The resolved part of molecular transport is handled by the gradient transport term, whereas the unresolved part of molecular mixing is handled by the micromixing model. This treatment of molecular diffusion allows differential diffusion effects to be accounted for and produces no spurious scalar variance when approaching the direct numerical simulation (DNS) limit [19,20].

The Vreman algebraic subgrid model [21] is used to compute the subgrid turbulent viscosity, which is given by

$$\bar{\Gamma}_t = C_v \sqrt{B_\beta / \left(\frac{\partial \bar{U}_j}{\partial x_i} \frac{\partial \bar{U}_j}{\partial x_i} \right)}$$

where $C_v = 2.5C_S^2$ with the Smagorinsky constant C_S is taken to be 0.1; and B_β is the second invariant of a tensor quantity, which was comprehensively described in Ref. [21]. The subgrid turbulent diffusivity is computed from the subgrid turbulent viscosity using a turbulent Schmidt number of 0.4 [22]. The value of 0.4 is not specifically optimized for this configuration; it has been applied to both non-premixed [22] and premixed [13] combustions in the context of the LES. The results presented in Appendix A illustrate that the simulation exhibits little sensitivity to the turbulent Schmidt number ranging from 0.4 to 0.6. The molecular diffusivity is computed using the unity Lewis number assumption; therefore, differential diffusion effects are not considered in this work. The mixing frequency Ω_M is modeled by the constant mixing rate parameter model:

$$\Omega_M = C_M \Omega_t = C_M (\bar{\Gamma} + \bar{\Gamma}_t) / \Delta^2 \quad (5)$$

where C_M is a model constant, $\Omega_t = (\bar{\Gamma} + \bar{\Gamma}_t) / \Delta^2$ is the subgrid turbulence frequency, and Δ is the filter width. The micromixing model ($\mathbf{M}(\phi)$) is taken to be either IEM [18] or EMST [23]. In the following contents, IEM is applied unless specifically stated.

The LES/FDF simulation employs a 16-species reduced mechanism, ARM1, for methane [24]. Detailed chemical mechanisms (e.g., GRI3.0 [25] and UCSD [26]) were found to yield similar predictions for this flame [10]. The viscosity and thermal diffusivity are computed as a function of a temperature using the curve fits given by Ref. [13], i.e., $\nu = \nu_0(T/T_0)^{1.69}$ and $\alpha = \alpha_0(T/T_0)^{1.71}$, where

$T_0 = 300$ K, $\nu_0 = 1.60 \times 10^{-5}$ m²/s, and $\alpha_0 = 2.24 \times 10^{-5}$ m²/s. These curve fits have been validated against the mixture-averaged transport properties from TRANLIB in CHEMKIN [27] for the methane-air mixture considered in this flame. The maximum error is less than 1% and is sufficiently accurate for the current LES/FDF simulation. Molecular diffusivity is obtained from the thermal diffusivity with the unity Lewis number assumption. The specific heat capacity is calculated using CKLIB in CHEMKIN [27]. The ideal gas law is applied as the equation of state. In situ adaptive tabulation (ISAT) [28,29] is applied to accelerate chemistry calculations, with the ISAT error tolerance being 6×10^{-6} . The results using half of the error tolerance (i.e., 3×10^{-6}) are presented in Appendix B to illustrate that further reducing the ISAT error tolerance below 6×10^{-6} has only a minor impact on predictions. The nominal number of computational particles per cell is 20, and the statistics are time averaged for 10 flowthrough times. These numerical settings have been extensively tested in Ref. [13] to ensure numerical accuracy. The mixing rate parameter C_M is 20.0 unless specifically stated. The cylindrical computational domain extends 60D in the axial direction, 24D in the radial direction, and 2π in the circumferential direction, where D is the central jet diameter of 4 mm. Three sets of grids have been employed, namely, G1 of $192 \times 96 \times 48$ cells, G2 of $256 \times 120 \times 64$ cells, and G4 of $256 \times 216 \times 64$ cells in the axial, radial, and circumferential directions, respectively. The inlet boundary conditions are taken to be the same as in Ref. [13]. Figure 1 shows a schematic plot of the inlet conditions and the approximated flame location in the computational domain.

The cylindrical domain is discretized by unevenly spaced grid points in the axial and radial directions. To illustrate the grid resolution in terms of the characteristic flame thermal thickness δ_L , the ratio of δ_L over the grid spacing in the axial (Δx) and radial (Δr)

directions is shown in Fig. 2a. The characteristic thermal thickness is 0.29 mm, which is computed as $\delta_L = (T_b - T_u) / \max(|\nabla T|)$ from the opposed jet flame of the central jet versus pilot streams with the maximum bulk strain rate before extinction. Note that T_b and T_u are the burned and unburned temperatures. As in Refs. [10,12,30], the opposed jet flame is chosen as reference because the tangential strain produced by the opposing streams mimics the effect of shear in the jet flame. As shown, there are about one and two radial cells per δ_L in the central jet region for G1 and G4, respectively. Therefore, the flame structure is not fully resolved, even with the finest grid. As for the axial resolution, there is about half of a cell per δ_L for G1, G2, and G4 before $x/D = 5.0$. Note that the prediction is less affected by the axial resolution, and the results in Appendix C show that doubling the axial resolution has only minor effects on species profiles. To further confirm that the LES/FDF simulations performed are not in the DNS limit of the flowfield, Fig. 2b shows the radial profiles of the ratio between the time-averaged subgrid turbulent diffusivity and the resolved molecular diffusivity (i.e., $\langle \tilde{\Gamma}_t / \tilde{\Gamma} \rangle$) at four axial locations. As shown, the ratio gets reduced by increasing grid resolution, but it is still on the order of unity even for the finest grid.

III. Species Distribution and Flame Structure Analysis

A. Time-Averaged Radial Profiles

Figure 3 shows the radial profiles of the time-averaged quantities. As shown, the central jet mixture fraction is well predicted throughout the domain. Good grid convergence in terms of $\langle \xi_j \rangle$ before $x/D = 30.0$ is observed, which is consistent with the previous findings for the nonreacting PM1-200 flame [13]. A slight variation in $\langle \xi_j \rangle$ is observed at $x/D = 45.0$ due to the changes in the combustion process, and therefore the mixing characteristics with the grid

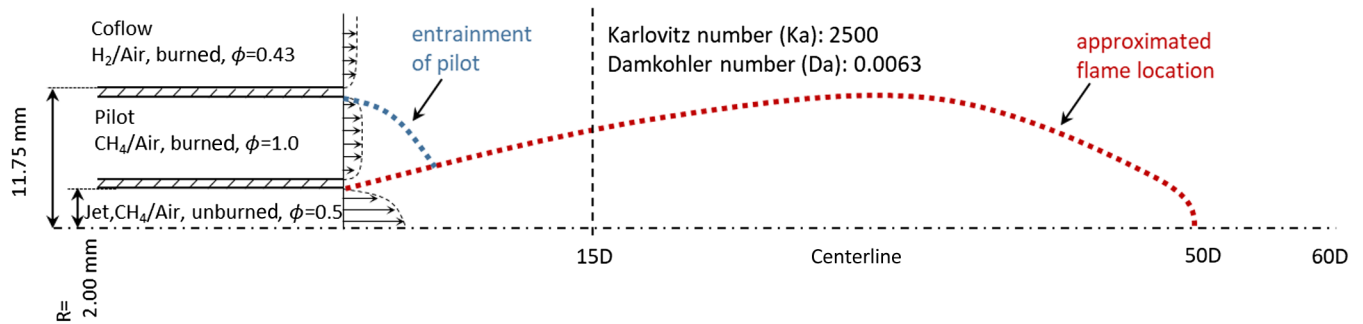


Fig. 1 Schematic plot of the inlet boundaries and approximated flame location in the computational domain.

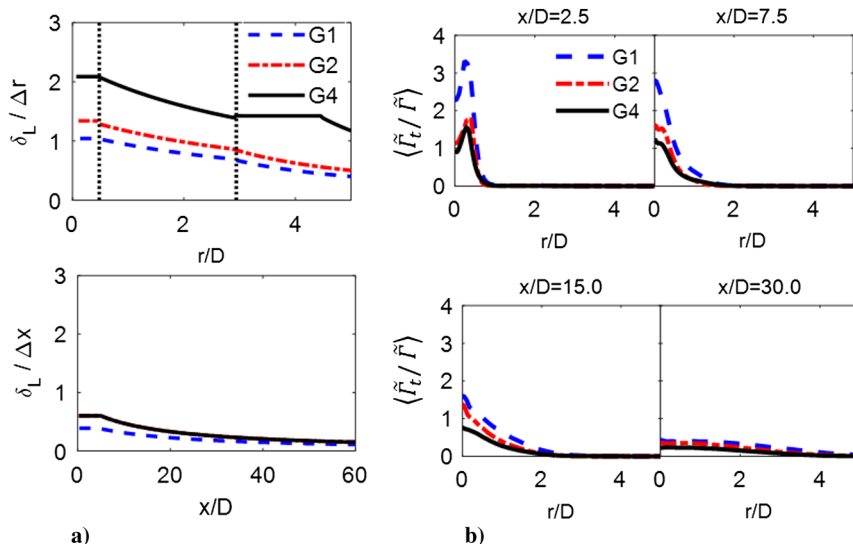


Fig. 2 Ratios of a) reference flame thickness over radial and axial grid space (dashed black lines denote boundaries of jet/pilot and pilot/coflow) and b) subgrid turbulent diffusivity over resolved molecular diffusivity.

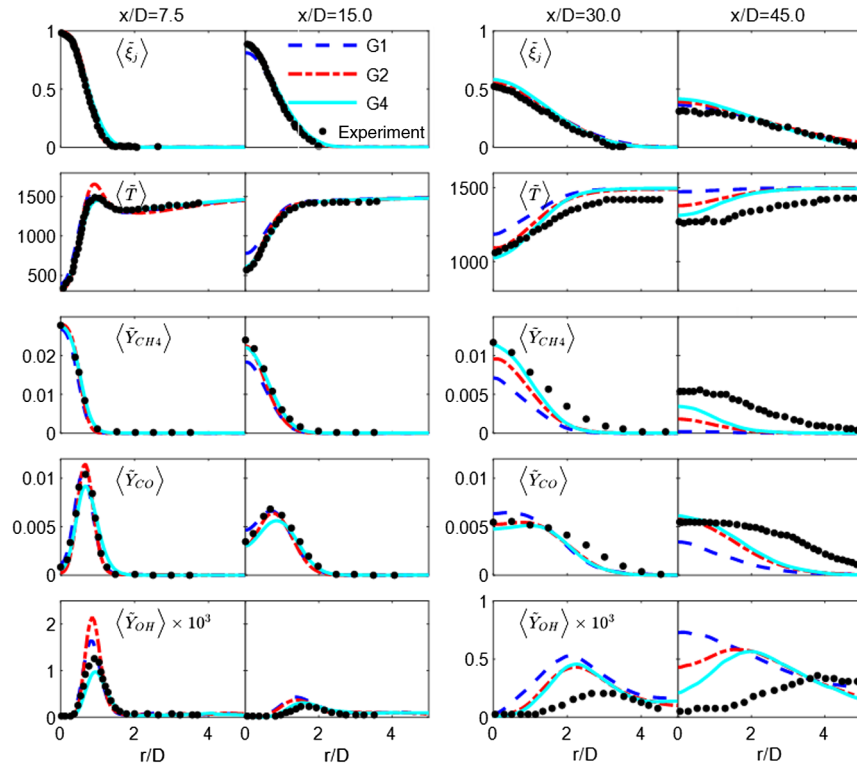


Fig. 3 Radial profiles of the time-averaged mean of the filtered central jet mixture fraction, temperature, and species mass fractions, with grids G1, G2, and G4.

resolution. As shown, reactive scalars such as methane (CH_4), carbon monoxide (CO), and hydroxyl radical (OH) are more sensitive to grid resolution. The simulation with G1, which well reproduces the results reported in Ref. [13], overpredicts the combustion process from $x/D = 15.0$; and the overprediction becomes more severe for the further downstream region, as indicated by the distribution of CH_4 and the temperature. Notable improvements for all the reactive scalars are obtained by increasing the grid resolution, with G4 yielding reasonable prediction of $\langle \tilde{T} \rangle$, $\langle \tilde{Y}_{\text{CH}_4} \rangle$, $\langle \tilde{Y}_{\text{CO}} \rangle$, and $\langle \tilde{Y}_{\text{OH}} \rangle$ up to $x/D = 30.0$. Figure 4 shows the predictions from some previous representative simulations (e.g., the RANS/PDF simulation in 2011 [10], the LES/flamelet simulation in 2013 [11], and the LES/FDF simulation in 2013 [13]) in comparison with the current simulation using the grid G4. The notable improvement highlights the pronounced effect of grid resolution for LES/FDF simulations of this highly turbulent jet flame. It is worth mentioning that all the simulations shown in Fig. 4 overpredict the coflow temperature by around 70 K. The investigation by Rowinski and Pope [13] illustrated that the influences of radiative heat loss and entrainment are minor. Therefore, the overprediction of the coflow temperature is likely due to the heat loss of the coflow stream to the burner near the inlet. This inlet

boundary issue only becomes evident downstream because it takes time for the coflow stream to get entrained into the area of $r/D < 5.0$. As preliminary tests for its potential influence, additional simulations using a lower inlet coflow temperature have been carried out; and the results are presented in Appendix D.

Figure 5 shows the radial profiles of the rms quantities. The rms of the mixture fraction reaches grid convergence, and it agrees well with the experimental measurement. In contrast, the rms of reactive scalars (e.g., temperature, CH_4 , and CO) exhibits a certain level of grid dependence, especially in the downstream region. Similar to the mean quantities, the increase in grid resolution, in general, improves the prediction of rms quantities.

To further quantify the improvements with respect to grid resolution, the errors of the time-averaged quantities are examined. The error of the mean temperature along the axis is defined as

$$\text{Err}(T_0(x)) = |\langle \tilde{T}_0(x) \rangle_{\text{simu}} - \langle \tilde{T}_0(x) \rangle_{\text{exp}}| / \sqrt{T_0'^2(x)}_{\text{exp}}$$

where $\langle \tilde{T}_0(x) \rangle$ and $\sqrt{T_0'^2(x)}$ represent the time-averaged filtered mean and rms of temperature along the axis, respectively. The red

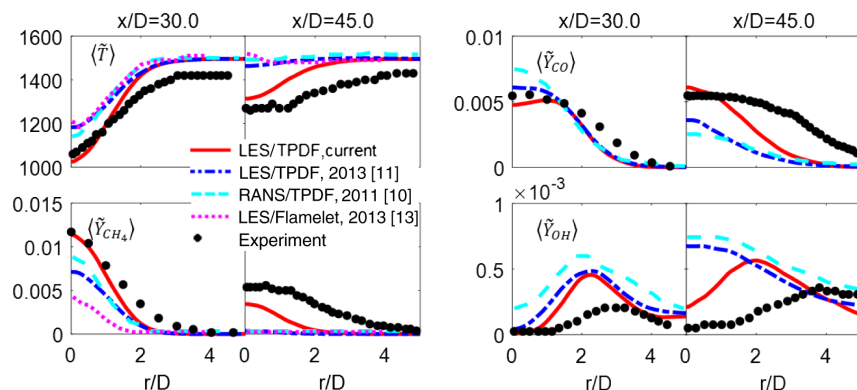


Fig. 4 Radial profiles of the time-averaged mean of the filtered temperature and species mass fractions in comparison with previous representative simulations.

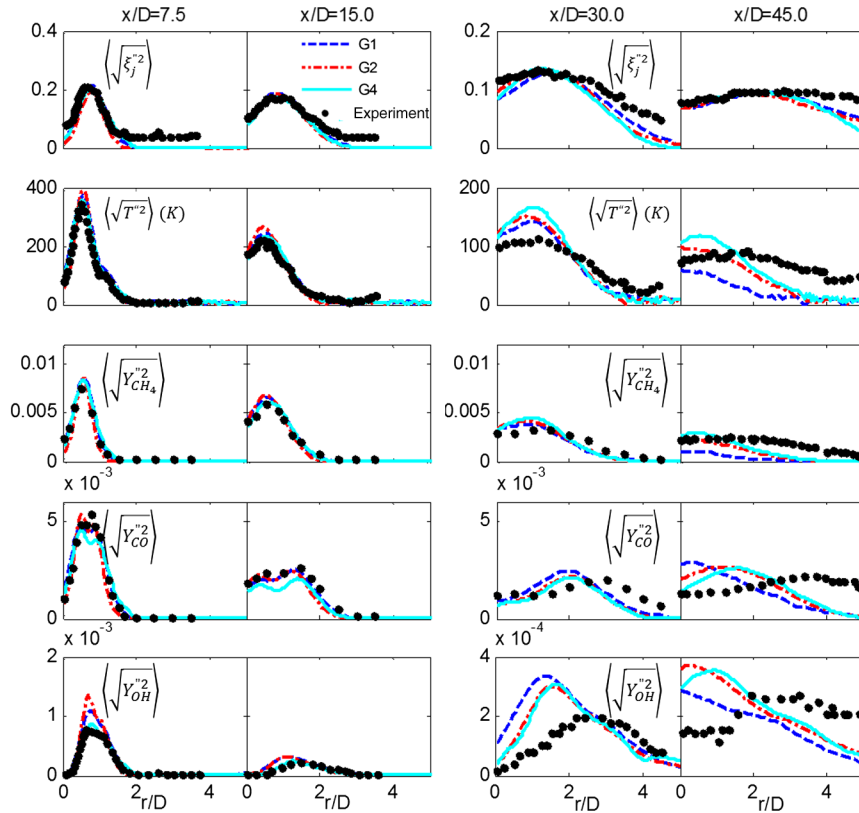


Fig. 5 Radial profiles of rms of the central jet mixture fraction, temperature, and species mass fractions, with grids G1, G2, and G4.

bars in Fig. 6 are the $Err(T_0(x))$ with grids G1, G2, and G4 at three representative locations. As shown, the error becomes larger in the downstream region due to the accumulated error all the way up to the inlet. Moreover, it is clear that, by increasing grid resolution from G1 to G2, the error of the temperature decreases significantly. Further increase of the grid resolution to G4 gains little improvement at $x/D = 15.0$ and 30.0 , but it reduces the error significantly at $x/D = 45.0$, where the error still exhibits sensitivity to grid resolution. To further quantify whether the primary source of discrepancy comes from the velocity field, large scalar mixing, or other factors, the errors of the mean mixture fraction [$Err(\xi_{j,0}(x))$] and velocity [$Err(U_0(x))$] are computed. As shown in Fig. 6, although $Err(T_0(x))$ becomes significantly larger further downstream, $Err(\xi_{j,0}(x))$ and $Err(U_0(x))$ are, in general, smaller and exhibit much less sensitivity to grid resolution. More important, the errors of the velocity and mixture fraction remain in the range from 0.1 to 0.5, even downstream, implying the accumulated errors in the velocity field and large-scale mixing are small. Figure 7 shows the $Err(T_0(x))$

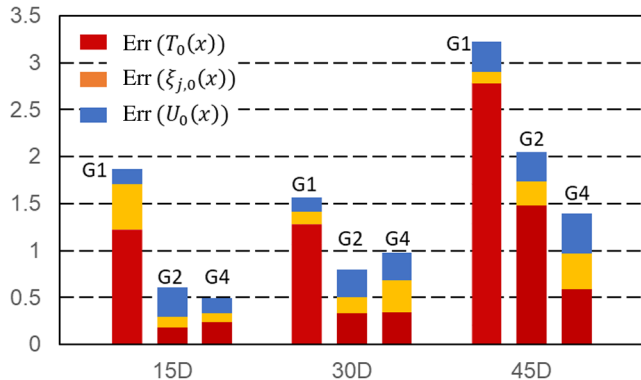


Fig. 6 Error of mean temperature ($Err(T_0(x))$), mixture fraction ($Err(\xi_{j,0}(x))$), and axial velocity ($Err(U_0(x))$) at $x/D = 15.0, 30.0,$ and 45.0 , with grids G1, G2, and G4.

against the filter size (Δ) on a log-log plot to examine the variation of errors in terms of grid resolution in a more quantitative manner. The filter size Δ is defined according to the local cubic volume, i.e., $\Delta = (\Delta x \times \Delta r \times r \Delta \theta)^{1/3}$. Also, r is taken to be $0.05D$ when computing Δ on the central axis. A line of slope = 2 is taken as the reference because the LES solver is second order in space. Note that, in addition to the spatial discretization error, many other errors (e.g., the statistical error from the Monte Carlo particle method, the operator splitting error when advancing the computational particles, and the error of chemistry integration from the ISAT method) may obscure the analysis on the order of accuracy because all the errors are coupled in a nonlinear fashion through the transport equations of reacting flows.

To illustrate that the accumulated errors in the velocity field are small, Fig. 8 shows the normalized mean axial velocity along the axis. As shown, both the coarsest grid (G1) and the finest grid (G4) match the experimental measurements reasonably well. Therefore, the discrepancy in the downstream region is most likely due to the

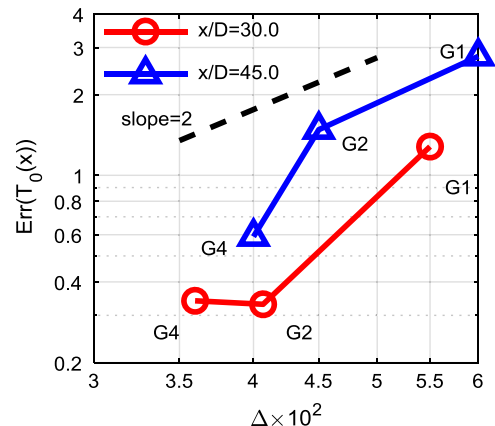


Fig. 7 Error of mean temperature ($Err(T_0(x))$) against the filter size (Δ) at $x/D = 30.0$ and 45.0 , with grids G1, G2, and G4.

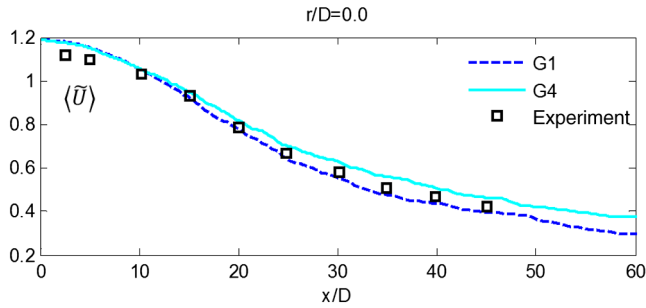


Fig. 8 Axial profile of the normalized mean axial velocity on the central axis with grids G1 and G4.

accumulated error resulting from the lack of resolution for reactive scalars rather than for velocity, which is further analyzed in Sec. IV.A.

B. Flame Structure Analysis

Figure 9 shows the contours of the instantaneous filtered progress variable \tilde{c} to illustrate the instantaneous flame structure, in which the progress variable is defined as the mass of the carbon element in carbon dioxide (CO_2) and CO over the total mass of the carbon element. The isolines of the filtered mixture fraction of 0.3 and 0.5 are shown as references. With grid G1, most of the regions with $\tilde{\xi}_j < 0.5$ are fully burned, as indicated by $\tilde{c} > 0.8$. By increasing resolution, the unburned regions (as indicated by $\tilde{c} < 0.2$) penetrate deeper into the downstream and spread more in the radial direction. And, most mixtures get fully burned only when $\tilde{\xi}_j$ is below 0.3. This indicates that, for a similar mixture composition, the combustion process becomes slower with the increase of grid resolution. It is interesting to note that there is a good correlation between the progress variable and the mixture fraction, indicating a certain level of transport similarity due to high turbulence, which is a useful implication for modeling these types of highly turbulent premixed flames.

To investigate the instantaneous flame structure more quantitatively, the conditional mean properties are extracted from computational particles and are compared to laminar reference flames with various bulk strain rates. Four cylindrical regions located at $x/D = 7.5, 15.0, 30.0,$ and 45.0 and within $0.0 < r/D < 2.0$ and $0 < \theta < 2\pi$ are selected as sample regions. The computational particles within these sampled regions are recorded for conditional statistics. The reference flames at each axial location are opposed jet flames composed of the central jet stream mixture versus the inert mixing product of pilot and coflow streams. For a laminar opposed jet flame to mimic the combustion characteristics of the turbulent flame considered,

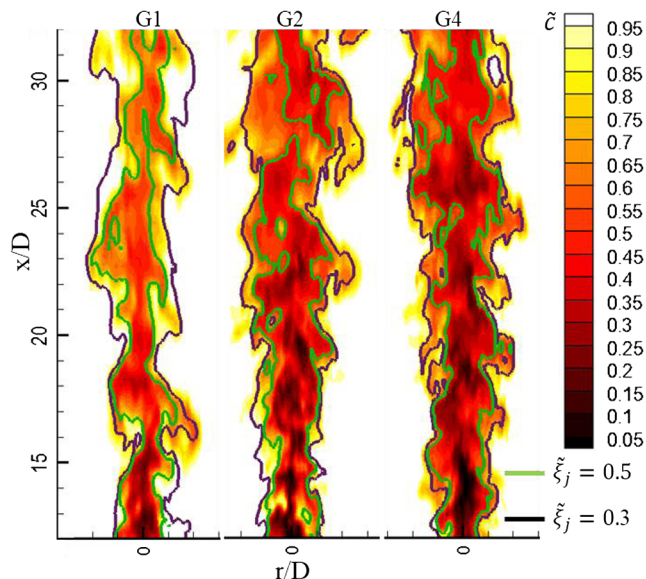


Fig. 9 Contours of the instantaneous filtered progress variable (\tilde{c}) from $x/D = 12.0$ to 32.0 . Also shown are the isolines of $\tilde{\xi}_j = 0.3$ and $\tilde{\xi}_j = 0.5$.

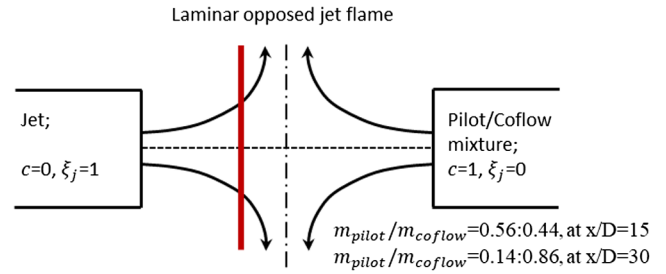


Fig. 10 Schematic plot of the laminar opposed jet flame configuration.

it is important to specify the pilot/coflow mixture that most intensively interacts with the central jet. This is done by calculating the centerline values of the pilot and coflow mixture fractions at the corresponding location [i.e., $\langle \tilde{\xi}_p(x, 0) \rangle$ and $\langle \tilde{\xi}_c(x, 0) \rangle$ based on C and H elements] and then inertly mixing the pilot and coflow streams with the mass fraction ratio $\langle \tilde{\xi}_p(x, 0) \rangle / \langle \tilde{\xi}_c(x, 0) \rangle$. A schematic plot of the laminar opposed jet flame configuration is shown in Fig. 10.

The pseudocolor in Fig. 11 represents the probability density function of the progress variable conditioned on the central jet mixture fraction $[f(c|\xi_j)]$ at $x/D = 15.0$. The $c - \xi_j$ profiles from laminar opposed flames under various bulk strain rates are drawn as references. The opposed flame with a bulk strain rate of 3150 s^{-1} corresponds to the laminar burning solution just before extinction. The pseudocolor illustrates that there is a considerable amount of mixtures below the laminar burning limit, indicating a level of local extinction and deviation from the laminar flame structure at this location. It is interesting to note that the luminosity observed from the experiment at this location is high. Meanwhile, Fig. 11 illustrates a considerable level of local extinction. This indicates that the high luminosity is mainly due to the effect of the hot pilot rather than the strong burning of the central jet. Figure 12 shows a similar plot at $x/D = 30.0$. As shown, the boundary of $f(c|\xi_j)$ sits well within the laminar opposed jet flame solutions with moderate bulk strain rates far from extinction. This indicates that the low luminosity observed in the experiment at this location is more of the characteristic of the laminar premixed flame composed of a very lean methane-air mixture rather than due to the local extinction. This finding is also consistent with the implication from the measured instantaneous CO and OH in Ref. [12]. For a further downstream region (e.g., at $x/D = 45.0$), the effect of stretch from turbulence further reduces, resulting in recovered flame luminosity. In addition, both Figs. 11 and 12 show that the upper and lower bounds of $f(c|\xi_j)$ move to lower values of c with grid G4 than with G1. This confirms the implication from Fig. 9 that, for the same mixture, the predicted combustion process becomes slower with the increased grid resolution.

The solid cyan lines in Figs. 11 and 12 represent the conditionally averaged c on ξ_j , i.e., $\langle c|\xi_j \rangle$ at $x/D = 15.0$ and 30.0 , respectively. In this study, a nominal flame thickness $\delta_L(x_0)$ is defined as the thermal thickness of the laminar opposed flame yielding the $c - \xi_j$ profile closest to the $\langle c(x_0)|\xi_j \rangle$ from the G4 simulation. As shown, the nominal flame thicknesses $\delta_L(x_0)$ are 0.37 mm at $x/D = 15.0$ and 0.75 mm at $x/D = 30.0$, respectively. Figure 13a shows the nominal flame thicknesses at $x/D = 7.5, 15.0, 30.0,$ and 45.0 , respectively. The nominal flame thickness increases along the axial location due to the relaxation of flame stretch by turbulence. Figure 13b shows the conditional mean of δ_L/Δ along the axial direction, which accounts for the streamwise variation of both δ_L and Δ . Note that only the computational cells within the combustion zone characterized by $0.05 \leq \tilde{c} \leq 0.95$ are sampled for statistics. As shown, $\langle \delta_L/\Delta|x \rangle$ becomes larger as it goes downstream; this indicates that δ_L increases faster than Δ along the axial direction, and it implies that the flame structure gets better resolved in the downstream region. Therefore, the deviation from the experimental measurement in the downstream region is more likely to be related to the accumulated error from upstream rather than the reduced grid resolution in the downstream region. It is further noticed from Fig. 13b that the number of computational grids per thermal flame thickness is mostly less than two,

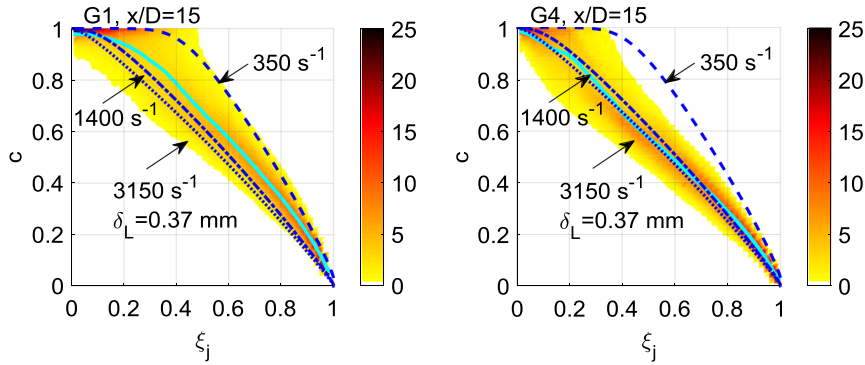


Fig. 11 Conditional PDFs of progress variable (pseudocolor) and conditional mean progress variable (solid line) at $x/D = 15.0$, and profiles of opposed laminar flames under different strain rates.

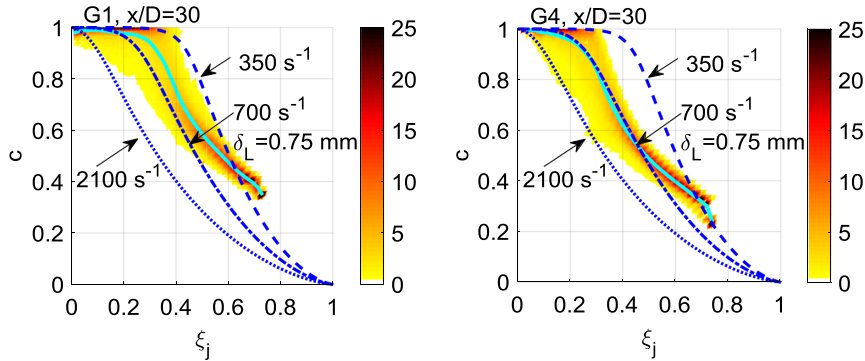


Fig. 12 Conditional PDFs of progress variable (pseudocolor) and conditional mean progress variable (solid line) at $x/D = 30.0$, and profiles of opposed laminar flames under different strain rates.

which is modest when considering that a well-resolved resolution requires ~ 20 grids, illustrating that the improved prediction due to the increase of grid resolution is not a simple consequence of approaching the DNS limit.

IV. Investigation on the Sources of Grid Sensitivity

The sources of grid sensitivity can be primarily attributed to the two unclosed terms in the particle evolution equations, namely, the subgrid turbulent transport term in Eq. (3) and the subgrid mixing term in Eq. (4). Furthermore, the notable improvement of the predicted species profiles with the increase of grid resolution can be attributed to three factors, i.e., the reduced importance of subgrid turbulent transport, the reduced importance, and/or more accurate modeling of subgrid mixing. In this section, the improved predictions by increasing grid resolution are thoroughly explained through the quantification of the resolved level of velocity and scalar fields, as well as the analysis of mixing-reaction budgets. Meanwhile, the most prominent factor for the large grid sensitivity is identified.

A. Resolved Level of Velocity and Scalar Fields

To explain the improved prediction by increasing grid resolution, the effects of increasing the grid resolution are investigated from the

perspective of the resolved level of velocity and scalar fields, which are quantified through the resolved ratios of turbulent kinetic energy and scalar variance, respectively. The resolved ratio of a scalar variance RR_ϕ , is defined as

$$RR_\phi = \frac{\langle \tilde{\phi}^2 \rangle - \langle \tilde{\phi} \rangle^2}{\langle \phi^2 \rangle - \langle \phi \rangle^2} \quad (6)$$

where $\langle \tilde{\phi}^2 \rangle - \langle \tilde{\phi} \rangle^2$ represents the resolved variance of ϕ , and $\langle \phi^2 \rangle - \langle \phi \rangle^2$ is the estimation for the total variance, as in Refs. [31,32]. When the simulation approaches the DNS limit, both $\langle \tilde{\phi}^2 \rangle$ and $\langle \tilde{\phi} \rangle^2 \rightarrow \langle \phi^2 \rangle$; meanwhile, $\langle \tilde{\phi} \rangle^2 \rightarrow \langle \phi \rangle^2$, resulting in $RR_\phi \rightarrow 1.0$. For turbulent kinetic energy, the resolved ratio is estimated as

$$RR_k = \frac{(1/2)(\langle \tilde{U}^2 \rangle - \langle \tilde{U} \rangle^2)}{(1/2)(\langle U^2 \rangle - \langle U \rangle^2) + (\nu_i/C\Delta)^2} \quad (7)$$

where \tilde{U} is the filtered streamwise velocity, and the resolved turbulent kinetic energy is estimated based on \tilde{U} . The subgrid turbulent kinetic

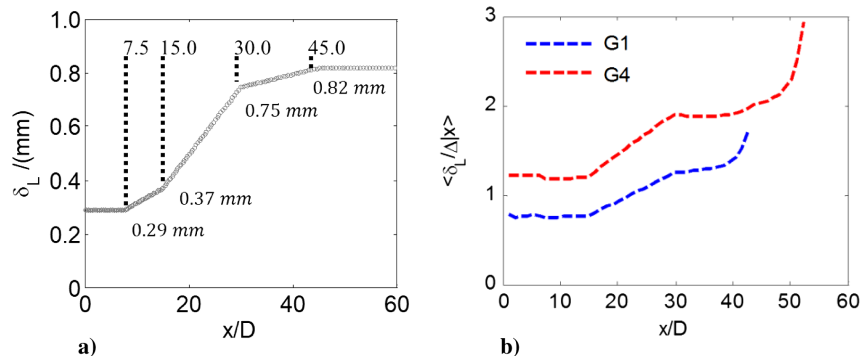


Fig. 13 Representations of a) reference flame thickness (δ_L) along the axial direction and b) grid resolution in terms of δ_L/Δ along the axial direction.

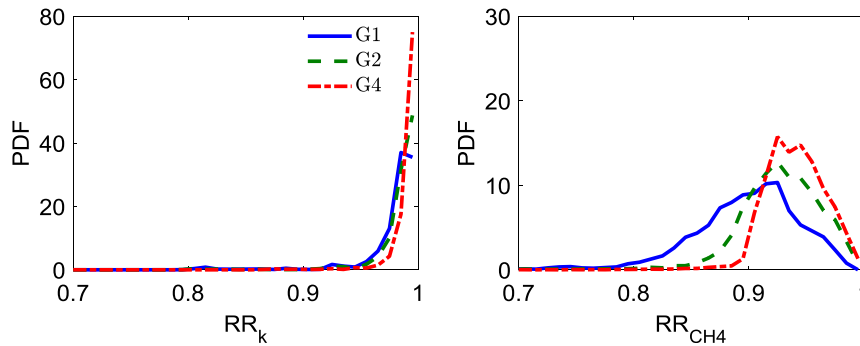


Fig. 14 PDFs of the resolved ratios of turbulent kinetic energy (RR_k) and Y_{CH_4} variance (RR_{CH_4}).

energy is estimated using $k_{sgs} = (\nu_t/C\Delta)^2$ with $C = 0.1$, as in Refs. [33,34]. Figure 14 shows the probability density functions (PDFs) of RR_k and RR_{CH_4} , which are obtained by taking the resolved ratio of each computational cell as a sample point, and then collecting these sample points within the combustion zone characterized by $0.05 \leq \tilde{c} \leq 0.95$ over the entire domain. As shown, more than 95% of the turbulent kinetic energy gets resolved even with the coarsest G1 grid, implying that the rms of the velocity field is relatively well resolved. This explains the grid convergence for the mean and rms of the mixture fraction, which is an indicator of the large-scale mixing. For reactive scalar fields, the resolved ratios exhibit notable grid sensitivity: the minimum resolved ratio of the Y_{CH_4} variance increases from 80 to 90% by increasing the grid resolution from G1 to G4. This indicates that the primary effect of increasing the grid resolution is on enhancing the resolved level of reactive scalars and that the subgrid turbulent transport has a minor impact, and is therefore not the primary source of grid sensitivity.

In turbulent premixed flames, chemical species may possess characteristic length scales, which are significantly different from each other [35]. Figure 15a shows the scatter of RR_{CH_4} versus RR_{OH} . Also drawn is a reference line of $RR_{CH_4}/RR_{OH} = 1.0$. The samples below the reference line imply that the variance of Y_{CH_4} is better resolved than that of Y_{OH} . The lower resolved ratio of OH may be attributed to its smaller characteristic length scale. With the increased resolution from G1 to G4, both RR_{CH_4} and RR_{OH} approach 1.0, with RR_{OH} (in general) being lower than RR_{CH_4} . For comparison, Fig. 15b shows the similar scatter plot obtained from the inert mixing simulation by suppressing the chemical reaction. The OH radical in this simulation is solely introduced from the pilot and coflow inlets. As shown, the scatter of RR_{CH_4} and RR_{OH} remains close to the reference line of $RR_{CH_4}/RR_{OH} = 1.0$ because the characteristic length scales of species are solely determined by turbulent mixing and are expected to be similar for all species. The notably lower RR_{OH} than RR_{CH_4} in the reacting flow simulation illustrates that the characteristic length scales imposed by flame structure are still significant in this highly turbulent premixed flame. This results in large sensitivity to the grid resolution even though the mean and rms of the velocity field are well resolved.

B. Mixing-Reaction Budgets

As demonstrated in the previous section, the primary effect of increasing the grid resolution is on reactive scalar fields. In LES/FDF simulations, for each individual particle, the species evolves according to Eq. (4), where the species net production rate results from resolved molecular diffusion, subgrid mixing, and chemical reaction. To investigate how these corresponding physiochemical processes vary with the increased grid resolution, the rates of change due to molecular diffusion, subgrid mixing, and chemical reaction are extracted from the corresponding fractional steps during the computation. Figure 16 shows the conditional budgets of progress variable at two selected locations of $x/D = 15.0$ and 30.0 . As shown, the resolved molecular diffusion is much smaller than the subgrid mixing, even with the finest grid G4. This illustrates that the conditional diffusion rate is predominantly modeled by the micromixing model; therefore, the improved prediction by increasing the grid resolution is most likely due to the more accurate modeling of subgrid mixing.

Further observation shows that there is a balance between the subgrid mixing and the reaction in the reaction zone (e.g., $c > 0.6$), illustrating the overall flame-propagation process in the PM1-150. This is consistent with the previous findings in RANS/PDF simulations [36]. More important, the increased resolution from G1 to G4 has more pronounced effects on subgrid mixing than on reaction, especially at downstream locations. For example, at $x/D = 30.0$, the peak of subgrid mixing in the reaction zone increases by about 60% in magnitude, whereas the peak of the reaction rate remains almost the same, resulting in a negative net production rate of the progress variable. Consequently, the overprediction of the combustion process gets alleviated, and better predictions of the species radial profiles are achieved. Therefore, the key factor for the improved prediction by increasing the grid resolution is the notably enhanced negative budget due to subgrid mixing. This points to the micromixing model as the largest source of grid sensitivity.

Figure 17 illustrates the uniformity of particle compositions by showing the normalized variance of progress variables, which is defined as $\eta = \tilde{c}'^2 / (\tilde{c}(1 - \tilde{c}))$, where \tilde{c}'^2 is the instantaneous subgrid variance reconstructed from the computational particles within individual cells. As shown, the maximum of η appears in the reaction

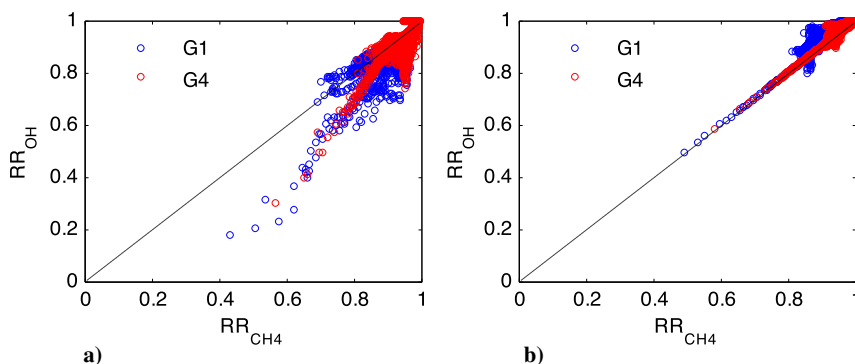


Fig. 15 Scatter plots of RR_{CH_4} versus RR_{OH} using grids G1 and G4: a) reacting simulations, and b) inert mixing simulations.

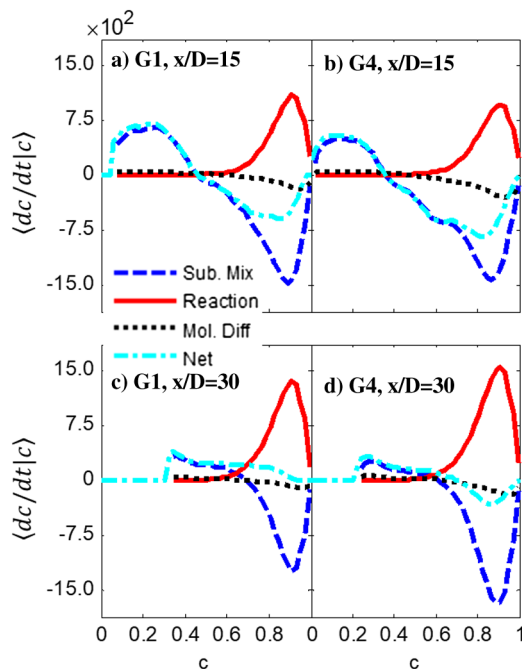


Fig. 16 Rates of subgrid mixing (Sub. Mix), chemical reaction (Reaction), molecular diffusion (Mol. Diff), and the summation (Net) conditionally averaged on the progress variable.

zone indicated by the regions where $0.6 < \tilde{c} < 0.9$. For grid G1, η could be over 0.15, implying that the simulation with $C_M = 20.0$ still exhibits significant subgrid variation and is still drastically different from the implicit LES in which the subgrid fluctuation is ignored and η is zero. By increasing the grid resolution from G1 to G4, the maximum value of η decreases by half, i.e., from 0.15 to 0.06. The increase of localness in composition space alleviates the modeling challenge for the IEM model, and thus improves the prediction.

V. Effects of Micromixing Modeling

The mixing-reaction budget analysis illustrates that the improved prediction by increasing the grid resolution can be primarily attributed to the enhancement of the negative budget due to subgrid mixing. In a TPDF simulation, the subgrid mixing rate is determined by the micromixing model, which usually consists of a specific mixing formulation describing the manner in which mixing occurs,

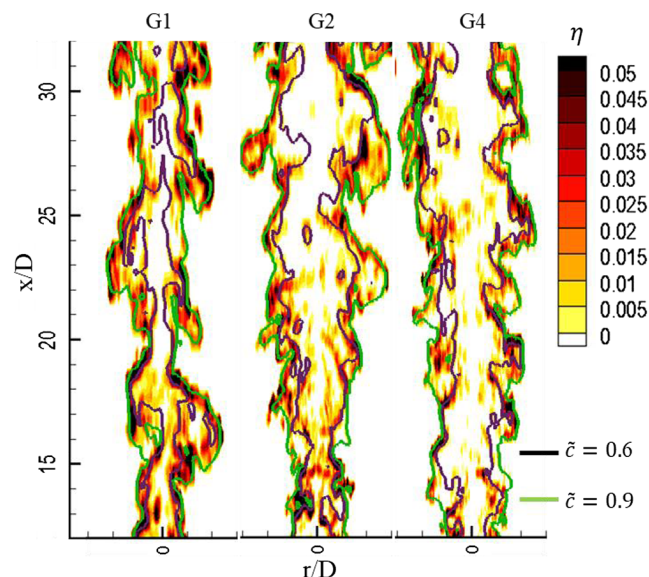


Fig. 17 Contours of the instantaneous normalized variance of the progress variable (η) from $x/D = 12.0$ to 32.0 . Also shown are the isolines of $\tilde{c} = 0.6$ and $\tilde{c} = 0.9$.

which is coupled with the specification of the scalar mixing timescale. In this section, the effects of the mixing timescale and mixing formulation are investigated through the analysis of mixing-reaction budgets and the conditional PDF of the progress variable. Alternative ways of modeling the mixing timescale and the mixing formulation are also employed to assess the performances among various models in terms of accuracy and grid sensitivity for LES/FDF simulations of this highly turbulent premixed flame.

A. Effects of Mixing Timescale

Previous studies on turbulent non-premixed combustion demonstrate the crucial impact of the scalar mixing timescale on the prediction of local extinction/reignition phenomena [37–39]. In the LES/FDF simulation of flame PM1-150 by Rowinski and Pope, the constant mixing rate parameter (C_M) was applied; and the improved predictions were obtained by increasing C_M from 5.0 to 20.0 [13]. It is important to appreciate that the turbulence timescale that the mixing rate parameter multiplies is different in the LES and in RANS. In the context of RANS, the turbulence timescale is at the integral scale, and the mixing rate parameter is (in general) on the order of unity. However, in the LES, the turbulence timescale is based on the subgrid quantities, resulting in a grid-dependent mixing rate parameter that can be much larger than unity. The dynamic modeling of C_M shows that this constant could be easily over 20.0 [40]. In this work, C_M is taken to be 5.0, 20.0, and 40.0 for parametric study. Figure 18 shows the radial profiles of the time-averaged quantities with different C_M values using grid G1. Consistent with the finding in Ref. [13], increasing C_M from 5.0 to 20.0 results in a notable improvement. Further increasing C_M beyond 20.0 has only a minor impact. It is worth mentioning that, different from many previous studies in which increasing the mixing frequency was shown to enhance the combustion progress [41–43], increasing C_M results in the suppression of the combustion progress in this highly turbulent flame. The finding about C_M is supported by the particle-level sensitivity analysis of another high-speed PPJB flame, i.e., flame PM1-200 in which the combustion progress is found to exhibit negative sensitivity to micromixing [36]. This is as expected because stronger mixing results in more extinction for a flame close to the blowoff limit.

To further reveal the effects of C_M variation on the subgrid physiochemical processes, a mixing-reaction budget analysis is performed for LES/FDF simulations on grid G1 with various C_M values. As shown in Fig. 19, similar to the grid refinement, the subgrid mixing yields a negative budget near $c = 1$ and a positive budget near $c = 0$, therefore diffusing the reaction progress away from the burned state to the unburned state. Meanwhile, larger negative net production rates are observed when C_M is increased from 5.0 to 20.0, which results in the alleviation of the overpredicted combustion process. However, different from grid refinement, both reaction and subgrid mixing rates of the progress variable are reduced by increasing C_M , demonstrating the compound effects of the scalar mixing timescale on the combustion process. It is further noticed that the magnitude of the subgrid mixing rate is reduced with the increase of C_M , despite the fact that a larger value of C_M corresponds to larger mixing frequency. This is because increasing C_M reduces the subgrid variance, which compensates for the increase of mixing frequency. A further increase of C_M to 40.0 has little impact on the net production rate of the progress variable, and consequently results in almost the same radial profiles as those with $C_M = 20.0$. It is worth noting that taking $C_M = 40.0$ on grid G1 yields a similar mixing frequency to taking $C_M = 20.0$ on grid G2. However, the latter one produces a notably better prediction of the species profile, implying that the modeling of the mixing timescale is not the only issue hindering the accurate prediction of this highly turbulent premixed flame. This points to further investigation on the mixing formulation.

B. Effects of Mixing Formulation

As a widely applied micromixing model with demonstrated success in predicting local extinction/reignition phenomena, the Euclidean minimum spanning tree model [23] is employed to investigate the effects of the mixing formulation on LES/FDF simulations of this

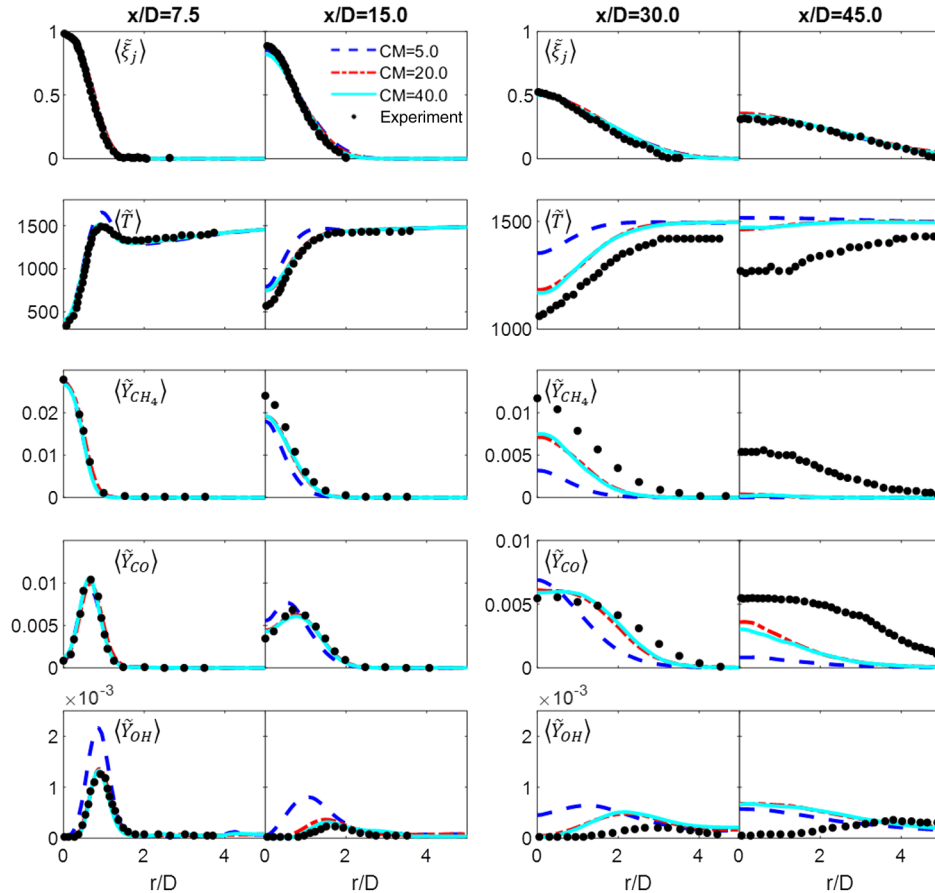


Fig. 18 Radial profiles of the time-averaged mean of the filtered central jet mixture fraction, temperature, and species mass fractions, with C_M of 5.0, 20.0, and 40.0.

highly turbulent premixed flame. A previous RANS/PDF investigation implied that the localness of mixing in the composition space may not be essential for high-speed PPJB flames [36]. However, in the LES context, the effects of enforcing localness in the composition space are unknown. In the following, the EMST model is applied with the mixing rate parameter of $C_M = 20.0$ to compare with the corresponding predictions using IEM. The results using the EMST with different C_M values are presented in Appendix E to illustrate that increasing C_M suppresses the combustion progress, which is the same as the findings from IEM. Figure 20 shows the time-averaged filtered mean and rms species radial profiles using the IEM and EMST models, respectively. As expected, there is no significant difference in $\langle \tilde{\xi}_j \rangle$ and $\langle \sqrt{\xi_j'^2} \rangle$ between the IEM and EMST models because subgrid mixing does not affect the mean of a passive scalar, and both models yield the exponential decay of subgrid variance at the same characteristic time of $1/\Omega_M$. The radial profiles of $\langle \tilde{T} \rangle$ and $\langle \tilde{Y}_{CH_4} \rangle$ illustrate that, under the same spatial resolution (together with the same mixing timescale), the EMST predicts a faster overall

combustion process than IEM. By increasing the grid resolution, both the IEM and EMST exhibit improvements on the predictions for reactive scalars. Moreover, the prediction using IEM exhibits larger sensitivity to grid resolution, especially in the downstream region, e.g., $\langle \tilde{T} \rangle$ and $\langle \tilde{Y}_{CH_4} \rangle$ at $x/D = 45.0$. The lower dependence on grid resolution for the EMST may be attributed to its localness in composition space.

To further investigate the behavior of the EMST model in this highly turbulent premixed flame, Fig. 21a shows the conditional PDF of progress variable ($f(c|\xi_j)$) from the EMST at $x/D = 15.0$ using grid G1 with the constant mixing rate parameter $C_M = 20.0$. Compared to the $f(c|\xi_j)$ predicted by IEM shown in Fig. 21b (reproduced from Fig. 11 to facilitate comparison), at the same value of ξ_j , both the upper and lower bounds of $f(c|\xi_j)$ move to higher values of c when the EMST is employed. In addition, the lower boundary of $f(c|\xi_j)$ sits well within the solution of the laminar opposed jet flame with a strain rate of 3150 s^{-1} , implying all the computational particles are within the burning solution. This is different from the predictions from the IEM model, where a significant number of computational

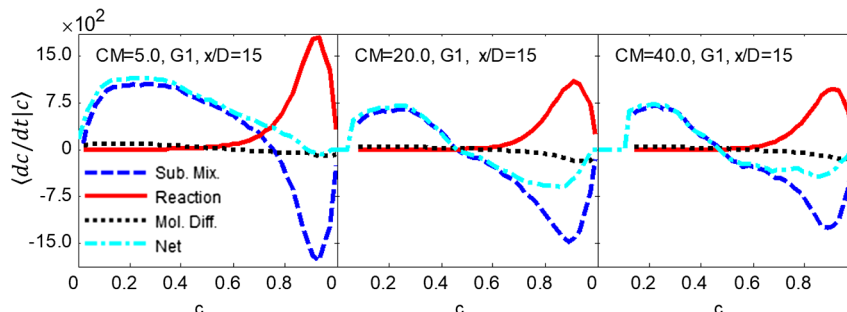


Fig. 19 Rates of subgrid mixing, reaction, molecular diffusion, and the summation conditionally averaged on the progress variable with $C_M = 5.0, 20.0,$ and 40.0 .

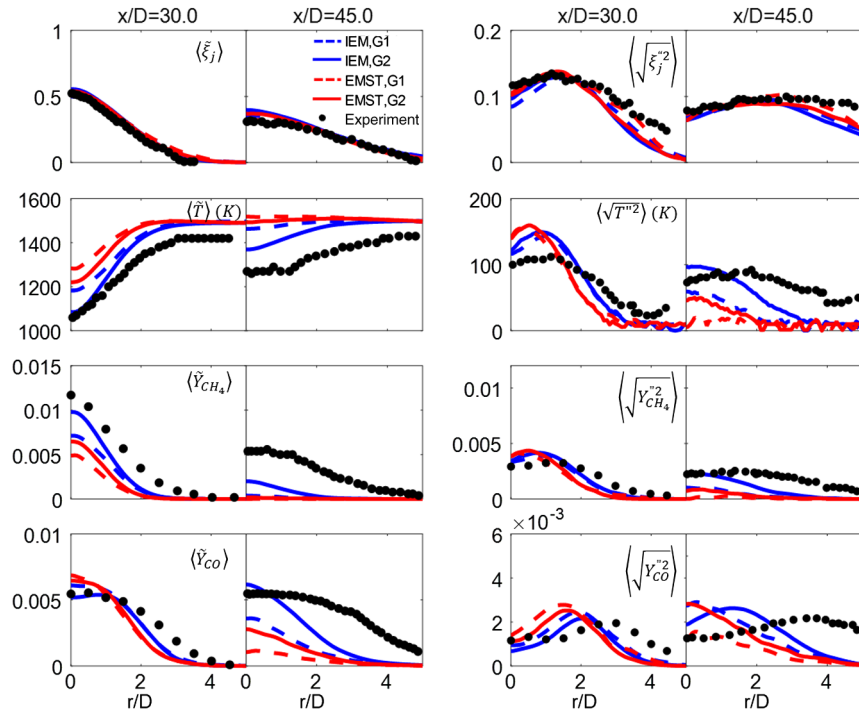


Fig. 20 Radial profiles of the time-averaged filtered mean and rms quantities using IEM and EMST models with grids G1 and G2.

particles are locally extinguished. Therefore, for this highly turbulent premixed flame, the EMST model predicts less extinction than the IEM model. The similar characteristics have been reported in turbulent non-premixed combustion [37–39,44], where the EMST was found to be more resistant to extinction. In terms of the conditional mean of the progress variable ($\langle c|\xi_j \rangle$), it is interesting to note that $\langle c|\xi_j \rangle$ is close to the laminar flame with the bulk strain rate of 1400 s^{-1} when IEM is applied. However, the bulk strain rate matching the $\langle c|\xi_j \rangle$ predicted by the EMST is as low as 350 s^{-1} . It has been demonstrated in Ref. [45] that, by neglecting the intermittency, the EMST model yields an equation similar to the unsteady flamelet equation, except that the mean scalar dissipation rate rather than the instantaneous one appears in that equation. Because the mean scalar dissipation rate may be much smaller than the instantaneous one, this may explain why the predicted $\langle c|\xi_j \rangle$ by the EMST corresponds to a laminar flame with a low strain rate. The finding implies that the EMST model may overenforce the localness in composition space for this highly turbulent premixed flame, providing valuable implications for further development of micromixing models.

The faster combustion process predicted by the EMST can also be implied from the subgrid mixing rate shown in Fig. 22. As observed, under the same grid resolution, the range of the positive subgrid mixing rate in progress variable space from the EMST is relatively wider than IEM, resulting in a faster combustion process. The negative budget due to subgrid mixing gets enhanced with the increased grid resolution, although less significant than IEM, resulting in the

alleviation of the overpredicted combustion process. These findings illustrate that both IEM and EMST models exhibit a certain level of dependence on grid resolution, resulting in large grid sensitivity for the LES/FDF simulation of this highly turbulent premixed flame. The development of a more advanced micromixing model and the assessment on some recently proposed models, such as the multiple-mapping conditioning model [46,47], the shadow-position mixing model [48,49], etc., warrant further study.

C. Discussion on an Alternative Mixing Timescale Model

Instead of modeling the scalar mixing timescale with the chemical reaction effect being completely ignored, a variety of mixing timescale models accounting for chemical reaction have been proposed for reactive scalar mixing [42,50–54] to yield the improved prediction of turbulent premixed flames. Among these, the hybrid mixing timescale model [54] linearly blends the expressions of scalar dissipation rates in the laminar flamelet and passive mixing limits, and it dynamically adjusts the mixing rate parameter according to the level of turbulence–chemistry interaction. This model was originally proposed for RANS/PDF simulations, and it has been validated against the DNS data of a lean premixed hydrogen–air jet flame, in which the model was found to be superior to the commonly used constant mechanical-to-scalar mixing timescale ratio model [54].

To investigate the potential improvement by accounting for the chemical reaction when modeling the mixing timescale in the LES/FDF simulation of this highly turbulent premixed flame, the hybrid

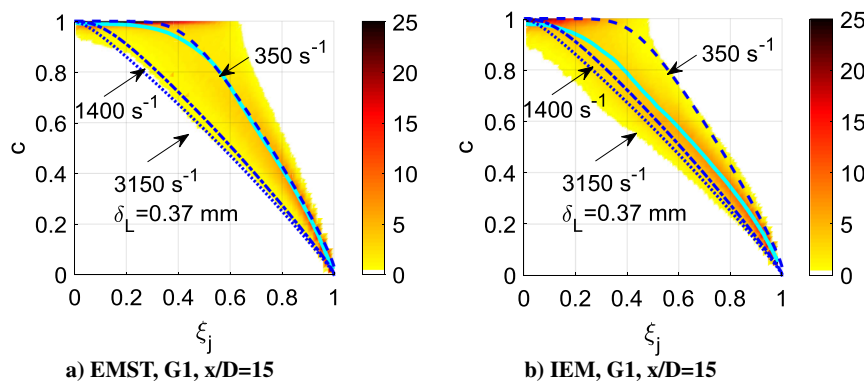


Fig. 21 Conditional PDFs of progress variable (pseudocolor) and conditional mean progress variable (solid line) predicted using EMST and IEM models.

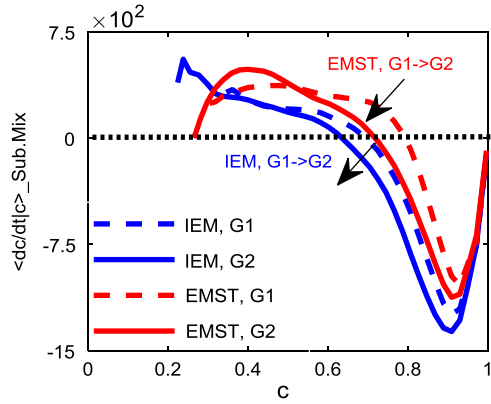


Fig. 22 Rates of subgrid mixing conditionally averaged on progress variable at $x/D = 30.0$ from the EMST and IEM models. $C_M = 20.0$ for all the calculations.

mixing timescale model is augmented to the LES context. A direct extension to the LES context by replacing the Reynolds-averaged quantities with the spatially filtered quantities yields

$$\Omega_M = (1 - \eta)C_M\Omega_t + \eta\tilde{\chi}_c^f/c'^{1/2} \quad (8)$$

where η is the subgrid segregation factor defined as the normalized variance of the progress variable, Ω_t is the subgrid turbulence frequency, and $\tilde{\chi}_c^f$ is the flame-induced scalar dissipation rate computed based on the laminar reference flames.

However, Eq. (8) does not yield the correct DNS limit of the flowfield, where turbulence gets fully resolved but not necessarily the flame structure. In this limit, the turbulence-induced mixing should approach zero. To account for the correct limiting behavior, the following attenuation factor is introduced:

$$\eta_a = 1 - e^{-\Delta/(al_\eta)} \quad (9)$$

where Δ is the filter width, l_η is the Kolmogorov length scale, and α is a model constant that is taken to be 1.0. Therefore, the augmented hybrid mixing timescale model for the LES is

$$\Omega_M = \eta_a(1 - \eta)C_M\Omega_t + (1 - \eta_a(1 - \eta))\tilde{\chi}_c^f/c'^{1/2} \quad (10)$$

such that, when $\Delta \ll l_\eta$, η_a approaches zero; and there is no turbulence-induced mixing. By introducing the extended segregation factor defined as $\eta^* = 1 - \eta_a(1 - \eta)$, Eq. (10) yields

$$\Omega_M = (1 - \eta^*)C_M\Omega_t + \eta^*\tilde{\chi}_c^f/c'^{1/2} = (1 - \eta^*)\Omega_c^t + \eta^*\Omega_c^f = \Omega_c^{\text{eff}} \quad (11)$$

where Ω_c^t , Ω_c^f , and Ω_c^{eff} correspond to the turbulence-induced, flame-induced, and effective mixing frequencies, respectively.

In this work, the laminar opposed jet flame of jet-coflow compositions with bulk strain rates of 700 s^{-1} is taken to be the reference flame for this model. This is because it best matches the conditional mean of progress variable ($\langle c|\xi_j \rangle$) at the downstream location of $x/D = 30$ (see Fig. 12). It is more valuable than matching $\langle c|\xi_j \rangle$ upstream, in the sense that the flame-induced mixing is expected to be more important downstream. The ratio Δ/l_η is estimated to be the order of one because $\Delta \sim \delta_L$ (as shown in Fig. 13) and $l_\eta \sim \delta_L$ (because the PM1-150 flame is close to the broken reaction zone regime [12]). For a parametric study, Δ/l_η is taken to be 1/3 and 2/1, with the corresponding η_a being 0.28 and 0.86, respectively. LES/FDF simulations are performed on grid G1 using both the constant mixing rate parameter model and the augmented hybrid timescale model with $C_M = 20.0$. As shown in Fig. 23, the hybrid mixing timescale model produces slightly better predictions of the species radial profiles. This is because, for this highly turbulent flame, the hybrid model (in general) has a minor impact on the scalar mixing

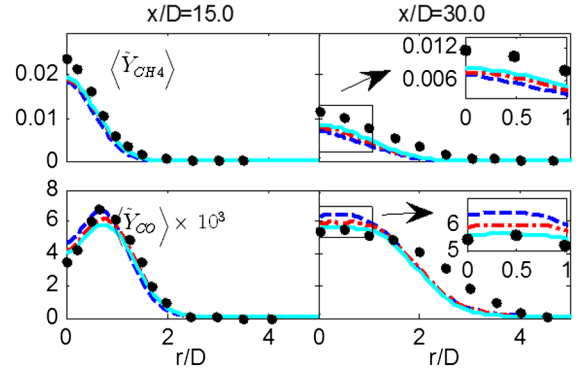


Fig. 23 Radial profiles of time-averaged filtered species mass fractions: constant $C_M = 20.0$ (dashed blue line); hybrid model with $\eta_a = 0.86$ (dotted-dashed red line); and hybrid model with $\eta_a = 0.28$ (solid cyan line).

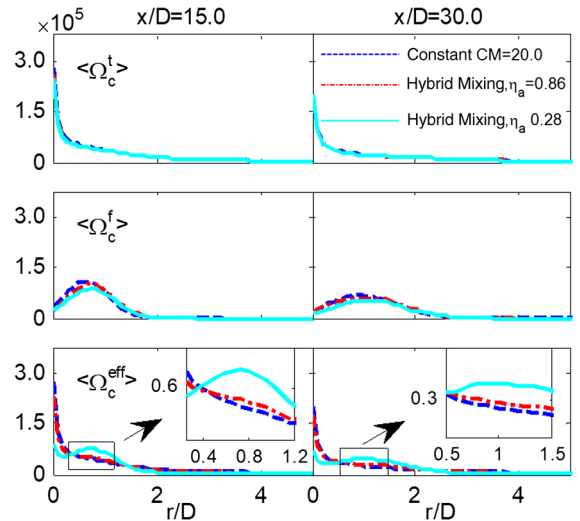


Fig. 24 Radial profiles of time-averaged turbulence induced mixing frequency, flame-induced mixing frequency, and effective mixing frequency.

timescale because it is mostly governed by turbulence. The flame-induced mixing frequency only exceeds the turbulence-induced mixing frequency in the flame brush between x/D of 15.0 and 30.0 (see Fig. 24 for the comparison of $\langle \Omega_c^t \rangle$, $\langle \Omega_c^f \rangle$, and $\langle \Omega_c^{\text{eff}} \rangle$), resulting in a slightly larger effective mixing frequency, and therefore a slight improvement of the species radial profiles. The major finding from applying the hybrid timescale model is that the scalar mixing timescale is mostly governed by turbulence for this highly turbulent flame, and the improvement by accounting for the chemical reaction in the mixing timescale modeling is small.

VI. Conclusions

LES/FDF simulations of the PM1-150 flame have been performed, which yielded notably improved predictions throughout the extinction-reignition region by increasing grid resolution. The comparisons between the molecular and subgrid turbulence diffusivities as well as the ratio between the filter size and the flame thermal thickness are made to demonstrate that the applied grid resolution is far from the DNS. Therefore, the improvement due to the increase of grid resolution is not a simple consequence of approaching the DNS limit. A flame structure analysis through the conditional PDFs of the progress variable shows that, at $x/D = 15.0$, there is a certain level of local extinction and deviation from the flamelet combustion regime. Meanwhile, beyond $x/D = 30.0$, the mixture sits well within the laminar burning solutions, demonstrating that the low luminosity at $x/D = 30.0$ is less related to local extinction.

The sources of grid sensitivity, which are primarily attributed to the two unclosed terms in the particle evolution equations (i.e., the subgrid turbulent transport term and the subgrid mixing term) are thoroughly examined through the quantification of the resolved levels of the velocity and scalar fields, as well as the mixing–reaction budget analysis. It is shown that more than 95% of the turbulent kinetic energy gets resolved even with the coarsest grid, implying that the subgrid turbulent transport has only a minor impact, and is therefore not the primary source of grid sensitivity. A mixing–reaction budget analysis illustrates that subgrid mixing dominates over the resolved molecular diffusion and is notably enhanced with the increased grid resolution. Therefore, the key factor for the improved prediction by the increasing the grid resolution is the more accurate modeling of subgrid mixing. This points to the micromixing model as the largest source of grid sensitivity. The instantaneous contours of the normalized subgrid variance of the progress variable further illustrate the increase of localness in the composition space with the increased grid resolution, which alleviates the modeling challenge for the micromixing model, and thus improves the predictions.

An investigation is carried out for the mixing timescale and the formulation, which are the two key components of a micromixing model. The effects of the mixing timescale are investigated through a parametric study of the mixing rate parameter and the analysis of mixing–reaction budgets. The results show that the subgrid mixing yields a negative production rate of the progress variable (c) near $c = 1$ and a positive rate near $c = 0$, therefore diffusing the reaction progress away from the burned state to the unburned state. Moreover, increasing C_M from 5.0 to 20.0 yields significant improvement due to the enhancement of the negative net production rate of the progress variable, illustrating that the mixing timescale is of paramount importance. However, the modeling of the mixing timescale is not the only issue hindering the accurate prediction of this highly turbulent premixed flame because grid G1 with $C_M = 40.0$ yields a similar

mixing frequency as grid G2 with $C_M = 20.0$, whereas the latter one produces notably better prediction. The effects of the mixing formulation are investigated through the comparison between IEM and EMST models. It is shown that the EMST is less grid dependent but predicts a notably faster combustion process as compared to IEM. The behaviors of these two models are explained through the mixing–reaction budgets and the conditional PDF of the progress variable, implying that the EMST may overenforce the localness in composition space for flame PM1-150. It is also shown that both IEM and EMST models exhibit a certain level of dependence on grid resolution, resulting in large grid sensitivity for the LES/FDF simulation of this highly turbulent premixed flame. Finally, the potential improvement by accounting for chemical reaction when modeling the mixing timescale is discussed. The recently proposed hybrid mixing timescale model is augmented for reactive scalar mixing in the LES context. The results show that, for PM1-150, the augmented hybrid model (in general) has a minor impact on the scalar mixing timescale because the turbulence (in general) controls the scalar mixing process. Only, for region $15.0 < x/D < 30.0$, a slightly larger mixing frequency is achieved by accounting for flame-induced mixing, which results in a slight improvement in the species radial profiles. These findings about grid sensitivity and micromixing models provide useful insights for the LES/FDF simulations of highly turbulent premixed flames.

Appendix A: Effects of Turbulent Schmidt Number

Figure A1 shows the radial profiles of the time-averaged quantities predicted with different values of the turbulent Schmidt number (S_{ct}) using grid G1 and $C_M = 20.0$. As shown, increasing S_{ct} slightly enhances the spreading of the central jet; but, in general, the difference due to the variation of S_{ct} is very minor. This minor difference can be expected from Fig. 2b, in which the molecular diffusivity is larger than turbulent diffusivity almost everywhere for $x > 15D$.

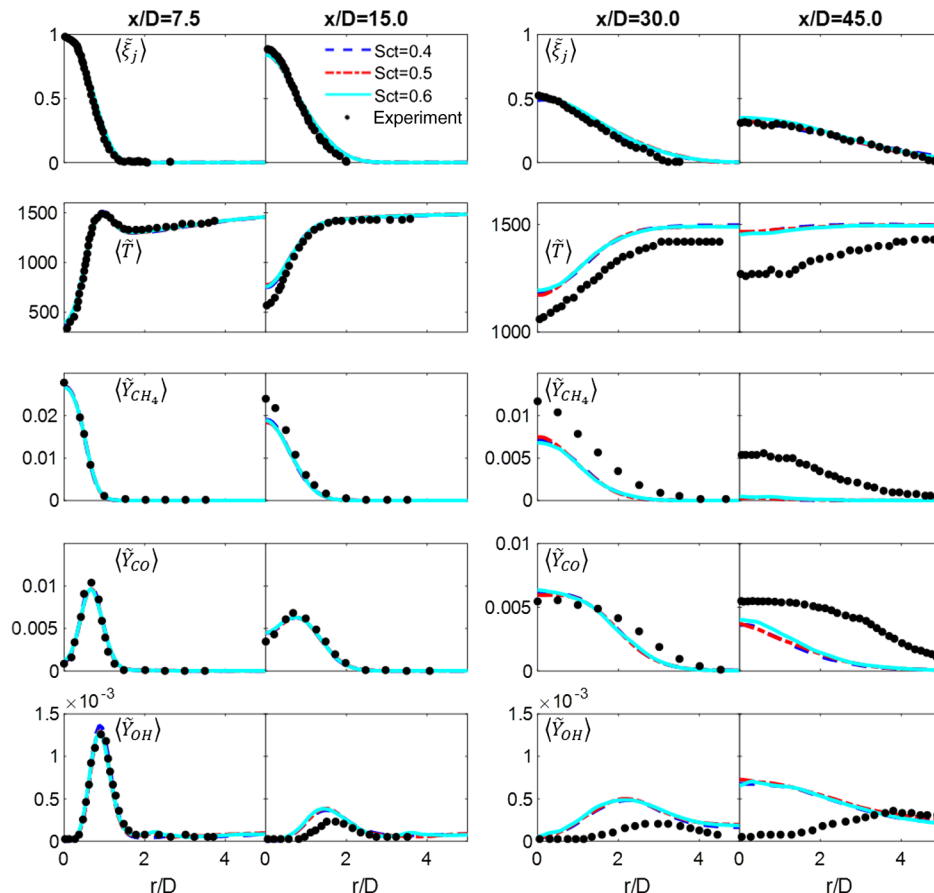


Fig. A1 Radial profiles of the time-averaged mean of the filtered central jet mixture fraction, temperature, and species mass fractions, with turbulent Schmidt numbers of 0.4, 0.5, and 0.6.

Appendix B: Effects of In Situ Adaptive Tabulation Error Tolerance

Figure B1 shows the radial profiles of the time-averaged quantities predicted with different ISAT error tolerances using the finest grid (G4) and $C_M = 20.0$. As shown, the results using half of the error tolerance (i.e., 3×10^{-6}) are very close to the baseline, illustrating that reducing the ISAT error tolerance below 6×10^{-6} has only a minor impact on predictions.

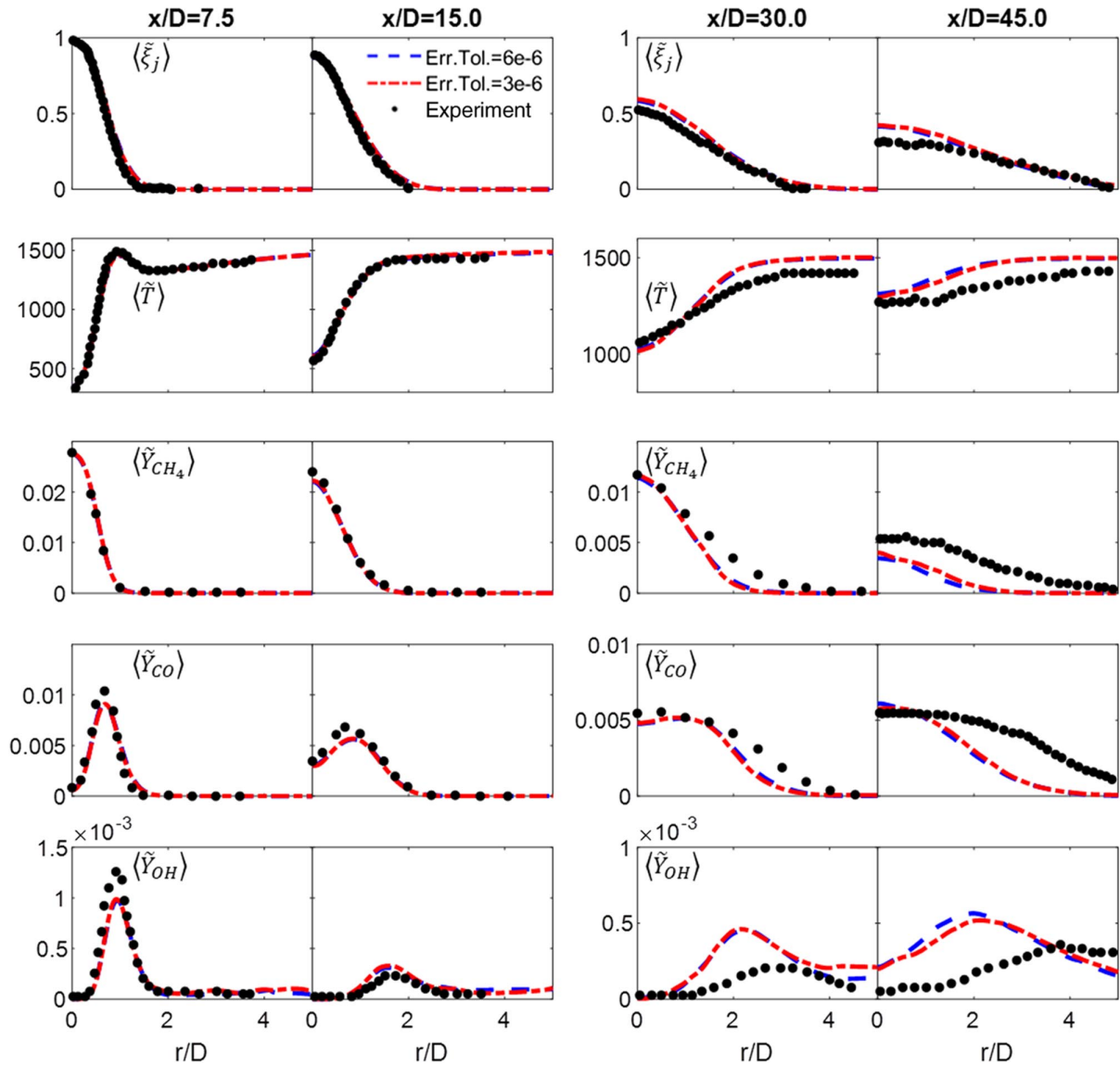


Fig. B1 Radial profiles of the time-averaged mean of the filtered central jet mixture fraction, temperature, and species mass fractions, with ISAT error tolerances (Err. Tol.) of 6e-6 and 3e-6.

Appendix C: Effects of Axial Grid Resolution

Figure C1 shows the radial profiles of the time-averaged quantities predicted using grid G1-A, which doubles the axial resolution of G1 but maintains its radial resolution. As shown, the improvement from G1 to G1-A is minor, illustrating that doubling the axial resolution has only minor effects on the scalar profiles and justifies the refinement in the radial direction from grids G2 to G4.

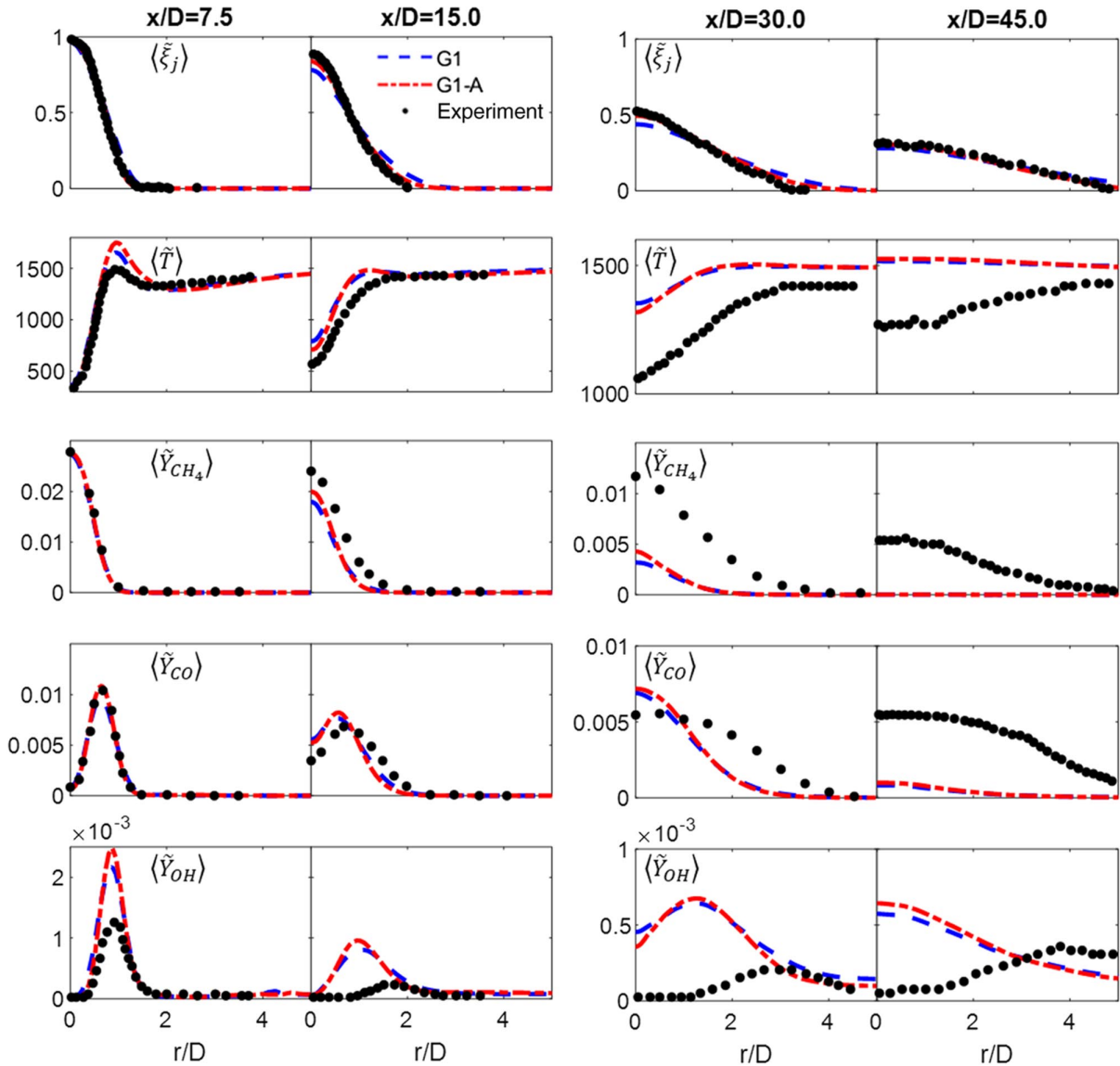


Fig. C1 Radial profiles of the time-averaged mean of the filtered central jet mixture fraction, temperature, and species mass fractions, with grids G1 and G1-A.

Appendix D: Effects of Coflow Temperature

Figure D1 shows the radial profiles of the time-averaged quantities predicted with a lower coflow temperature of 1430 K using the finest grid (G4) and $C_M = 20.0$. As shown, compared to the baseline value of 1500 K, the overprediction of the temperature and OH downstream gets notably suppressed. However, the discrepancies in CH_4 and CO profiles are still significant, implying that there are other factors causing the deviation.

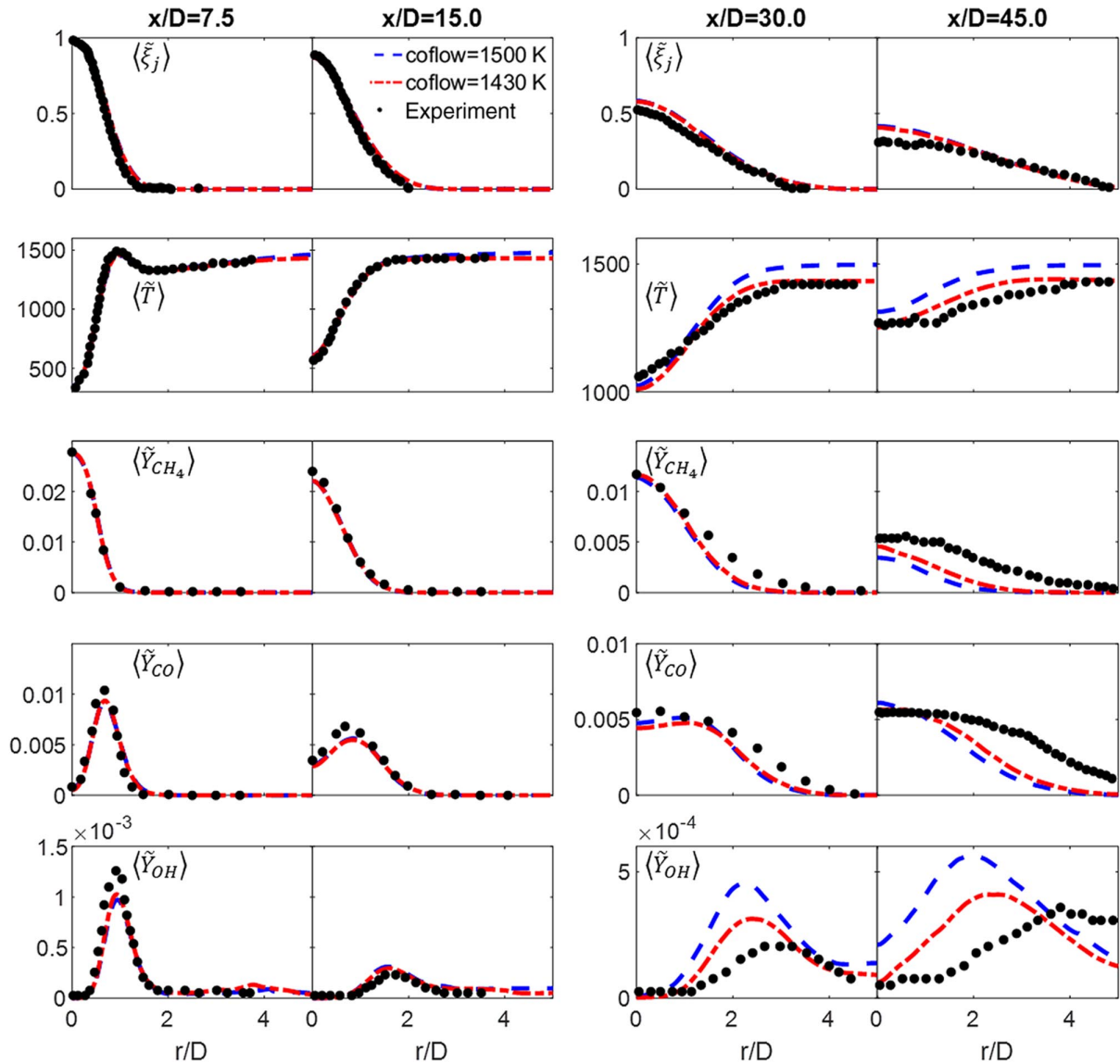


Fig. D1 Radial profiles of the time-averaged mean of the filtered central jet mixture fraction, temperature, and species mass fractions, with coflow temperatures of 1430 and 1500 K.

Appendix E: Effects of Mixing Rate Parameter

Figure E1 shows the radial profiles of the time-averaged quantities predicted with different values of C_M using the EMST model on grid G1. As shown, increasing C_M from 5.0 to 20.0 results in notable improvement, but further increasing C_M beyond 20.0 has only a minor impact. In general, increasing C_M suppresses the predicted combustion progress using the EMST. This is the same as the finding from IEM.

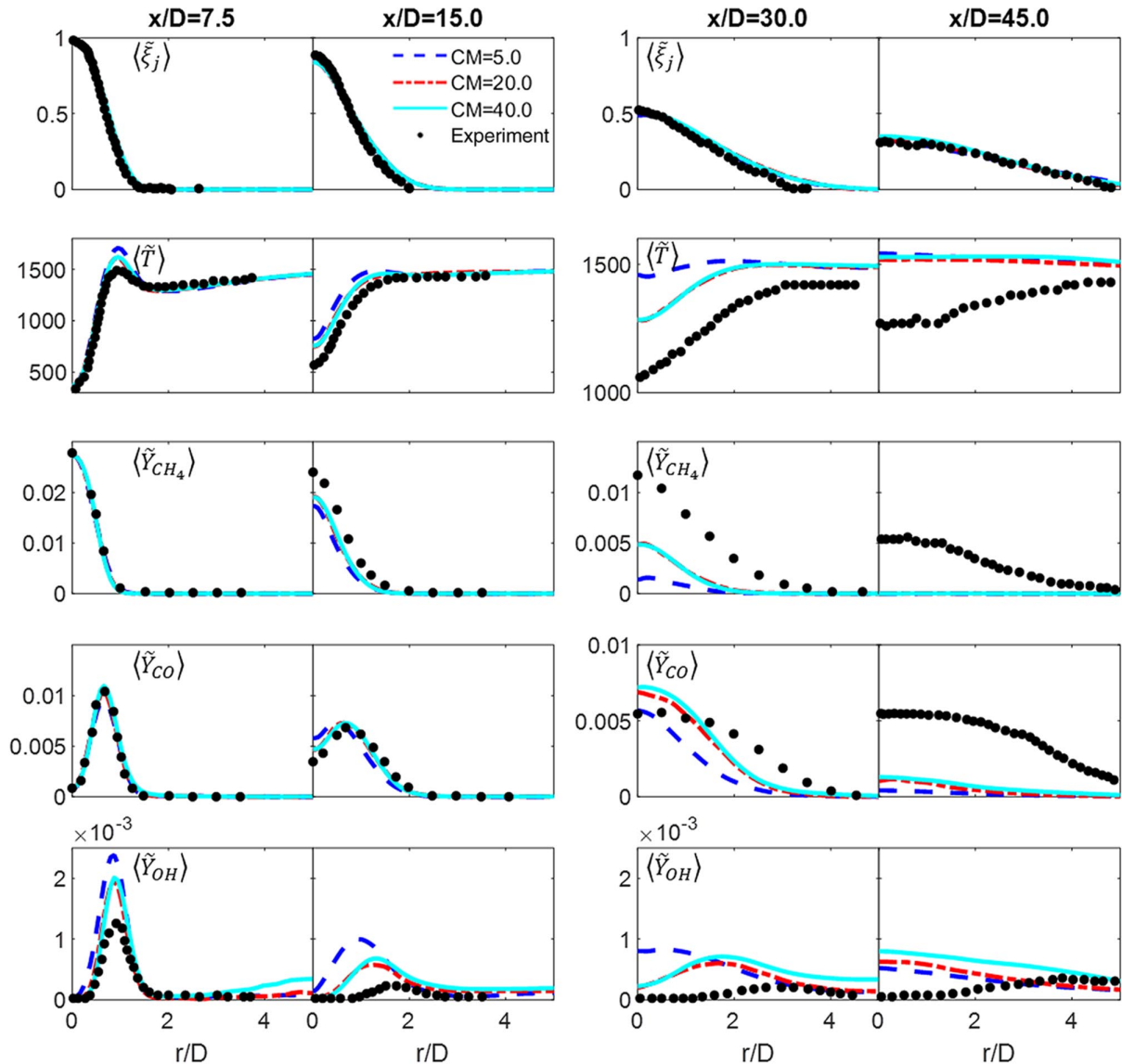


Fig. E1 Radial profiles of the time-averaged mean of the filtered central jet mixture fraction, temperature, and species mass fractions, using the EMST model with C_M of 5.0, 20.0, and 40.0.

Acknowledgments

The work is supported by National Natural Science Foundation of China (91841302) and the National Science and Technology Major Project (2017-I-0004-0005). This research at Cornell University is funded by the U.S. Department of Energy, Office of Science, Office of Basic Energy Sciences under award number DEFG02-90 ER14128. Simulations were done with the computational resources from the Tsinghua National Laboratory for Information Science and Technology.

References

[1] Bradley, T., and Fadok, J., “Advanced Hydrogen Turbine Development Update,” *ASME Turbo Expo 2009: Power for Land, Sea, and Air*, Vol. 1, American Soc. of Mechanical Engineers, Fairfield, NJ, 2009, pp. 349–356.
<https://doi.org/10.1115/GT2009-59105>

[2] Correa, S. M., “A Review of Nox Formation Under Gas-Turbine Combustion Conditions,” *Combustion Science and Technology*, Vol. 87, Nos. 1–6, 1993, pp. 329–362.
<https://doi.org/10.1080/00102209208947221>

[3] Barnes, J., and Mellor, A., “Effects of Unmixedness in Piloted-Lean Premixed Gas-Turbine Combustors,” *Journal of Propulsion and Power*, Vol. 14, No. 6, 1998, pp. 967–973.
<https://doi.org/10.2514/2.5361>

[4] Cohen, J. M., Wake, B. E., and Choi, D., “Investigation of Instabilities in a Lean, Premixed Step Combustor,” *Journal of Propulsion and Power*, Vol. 19, No. 1, 2003, pp. 81–88.
<https://doi.org/10.2514/2.6083>

[5] Venkataraman, K., Preston, L., Simons, D., Lee, B., Lee, J., and Santavicca, D., “Mechanism of Combustion Instability in a Lean Premixed Dump Combustor,” *Journal of Propulsion and Power*, Vol. 15, No. 6, 1999, pp. 909–918.
<https://doi.org/10.2514/2.5515>

[6] Dunn, M. J., Masri, A. R., and Bilger, R. W., “A New Piloted Premixed Jet Burner to Study Strong Finite-Rate Chemistry Effects,” *Combustion and Flame*, Vol. 151, No. 1, 2007, pp. 46–60.
<https://doi.org/10.1016/j.combustflame.2007.05.010>

[7] Dunn, M. J., Masri, A. R., Bilger, R. W., Barlow, R. S., and Wang, G. H., “The Compositional Structure of Highly Turbulent Piloted Premixed Flames Issuing into a Hot Coflow,” *Proceedings of the Combustion*

- Institute*, Vol. 32, No. 2, 2009, pp. 1779–1786.
<https://doi.org/10.1016/j.proci.2008.08.007>
- [8] Duwig, C., Nogenmyr, K. J., Chan, C. K., and Dunn, M. J., “Large Eddy Simulations of a Piloted Lean Premix Jet Flame Using Finite-Rate Chemistry,” *Combustion Theory and Modelling*, Vol. 15, No. 4, 2011, pp. 537–568.
<https://doi.org/10.1080/13647830.2010.548531>
- [9] Prasad, V. N., Luo, K. H., and Jones, W. P., “LES-PDF Simulation of a Highly Sheared Turbulent Piloted Premixed Flame,” *7th Mediterranean Combustion Symposium*, Associazione Sezione Italiana del Combustion Institute, Sardinia, Italy, 2011, pp. 11–15.
- [10] Rowinski, D. H., and Pope, S. B., “PDF Calculations of Piloted Premixed Jet Flames,” *Combustion Theory and Modelling*, Vol. 15, No. 2, 2011, pp. 245–266.
<https://doi.org/10.1080/13647830.2010.535568>
- [11] Chen, Y., and Ihme, M., “Large-Eddy Simulation of a Piloted Premixed Jet Burner,” *Combustion and Flame*, Vol. 160, No. 12, 2013, pp. 2896–2910.
<https://doi.org/10.1016/j.combustflame.2013.07.009>
- [12] Dunn, M. J., Masri, A. R., Bilger, R. W., and Barlow, R. S., “Finite Rate Chemistry Effects in Highly Sheared Turbulent Premixed Flames,” *Flow Turbulence and Combustion*, Vol. 85, Nos. 3–4, 2010, pp. 621–648.
<https://doi.org/10.1007/s10494-010-9280-5>
- [13] Rowinski, D. H., and Pope, S. B., “Computational Study of Lean Premixed Turbulent Flames Using RANS-PDF and LES-PDF Methods,” *Combustion Theory and Modelling*, Vol. 17, No. 4, 2013, pp. 610–656.
<https://doi.org/10.1080/13647830.2013.789929>
- [14] Wang, H., and Pope, S. B., “Large Eddy Simulation/Probability Density Function Modeling of a Turbulent CH₄/H₂/N₂ Jet Flame,” *Proceedings of the Combustion Institute*, Vol. 33, No. 1, 2011, pp. 1319–1330.
<https://doi.org/10.1016/j.proci.2010.08.004>
- [15] Yang, Y., Wang, H., Pope, S. B., and Chen, J. H., “Large-Eddy Simulation/Probability Density Function Modeling of a Non-Premixed CO/H₂ Temporally Evolving Jet Flame,” *Proceedings of the Combustion Institute*, Vol. 34, No. 1, 2013, pp. 1241–1249.
<https://doi.org/10.1016/j.proci.2012.08.015>
- [16] Popov, P. P., Wang, H., and Pope, S. B., “Specific Volume Coupling and Convergence Properties in Hybrid Particle/Finite Volume Algorithms for Turbulent Reactive Flows,” *Journal of Computational Physics*, Vol. 294, Aug. 2015, pp. 110–126.
<https://doi.org/10.1016/j.jcp.2015.03.001>
- [17] Pierce, C. D., and Moin, P., “Progress-Variable Approach for Large-Eddy Simulation of Non-Premixed Turbulent Combustion,” *Journal of Fluid Mechanics*, Vol. 504, No. 504, 2004, pp. 73–97.
<https://doi.org/10.1017/S0022112004008213>
- [18] Villermaux, J., and Devillon, J. C., “Représentation De La Coalescence Et De La Redispersion Des Domaines De Ségrégation Dans Un Fluide Par Un Modèle D’Interaction Phénoménologique,” *Proceedings of the 2nd International Symposium on Chemical Reaction Engineering*, Elsevier, New York, 1972, pp. 1–13.
- [19] McDermott, R., and Pope, S. B., “A Particle Formulation for Treating Differential Diffusion in Filtered Density Function Methods,” *Journal of Computational Physics*, Vol. 226, No. 1, 2007, pp. 947–993.
<https://doi.org/10.1016/j.jcp.2007.05.006>
- [20] Tirunagari, R. R., and Pope, S. B., “LES/PDF for Premixed Combustion in the DNS Limit,” *Combustion Theory and Modelling*, Vol. 20, No. 5, 2016, pp. 1–32.
<https://doi.org/10.1080/13647830.2016.1188991>
- [21] Vreman, A. W., “An Eddy-Viscosity Subgrid-Scale Model for Turbulent Shear Flow: Algebraic Theory and Applications,” *Physics of Fluids*, Vol. 16, No. 10, 2004, pp. 3670–3681.
<https://doi.org/10.1063/1.1785131>
- [22] Pitsch, H., and Steiner, H., “Large-Eddy Simulation of a Turbulent Piloted Methane/Air Diffusion Flame (Sandia Flame D),” *Physics of Fluids*, Vol. 12, No. 10, 2000, pp. 2541–2554.
<https://doi.org/10.1063/1.1288493>
- [23] Subramaniam, S., and Pope, S. B., “A Mixing Model for Turbulent Reactive Flows Based on Euclidean Minimum Spanning Trees,” *Combustion and Flame*, Vol. 115, No. 4, 1998, pp. 487–514.
[https://doi.org/10.1016/S0010-2180\(98\)00023-6](https://doi.org/10.1016/S0010-2180(98)00023-6)
- [24] Sung, C. J., Law, C. K., and Chen, J. Y., “An Augmented Reduced Mechanism for Methane Oxidation with Comprehensive Global Parametric Validation,” *Proceedings of the Combustion Institute*, Vol. 27, No. 1, 1998, pp. 295–304.
[https://doi.org/10.1016/S0082-0784\(98\)80416-5](https://doi.org/10.1016/S0082-0784(98)80416-5)
- [25] Smith, G. P., Golden, D. M., Frenklach, M., Moriarty, N. W., Eiteneer, B., Goldenberg, M., Bowman, C. T., Hanson, R. K., Song, S., Gardiner, W. C., et al., “The Gri-Mech 3.0,” (online database), Univ. of California, Berkeley, <http://combustion.berkeley.edu/gri-mech/version30/text30.html> [retrieved 15 Jan. 2020].
- [26] “The San Diego Mechanism,” (online database), Univ. of California, San Diego, La Jolla, CA, <http://web.eng.ucsd.edu/mae/groups/combustion/mechanism.html> [retrieved 15 Jan. 2020].
- [27] Kee, R. J., Dixon-lewis, G., Warnatz, J., Coltrin, M. E., and Miller, J. A., “A Fortran Computer Code Package for the Evaluation of Gas-Phase, Multicomponent Transport Properties,” Sandia National Labs. Rept. SAND86-8246, Livermore, CA, 1986.
- [28] Pope, S. B., “Computationally Efficient Implementation of Combustion Chemistry Using In Situ Adaptive Tabulation,” *Combustion Theory and Modelling*, Vol. 1, No. 1, 1997, pp. 41–63.
<https://doi.org/10.1080/713665229>
- [29] Lu, L., and Pope, S. B., “An Improved Algorithm for In Situ Adaptive Tabulation,” *Journal of Computational Physics*, Vol. 228, No. 2, 2009, pp. 361–386.
<https://doi.org/10.1016/j.jcp.2008.09.015>
- [30] Sankaran, R., Hawkes, E. R., Chen, J. H., Lu, T., and Law, C. K., “Structure of a Spatially Developing Turbulent Lean Methane–Air Bunsen Flame,” *Proceedings of the Combustion Institute*, Vol. 31, No. 1, 2007, pp. 1291–1298.
<https://doi.org/10.1016/j.proci.2006.08.025>
- [31] Poinso, T., and Veynante, D., *Theoretical and Numerical Combustion*, R.T. Edwards, Philadelphia, PA, 2005, pp. 174–176.
<https://doi.org/10.1016/j.combustflame.2005.11.002>
- [32] Vervisch, L., Domingo, P., Lodato, G., and Veynante, D., “Scalar Energy Fluctuations in Large-Eddy Simulation of Turbulent Flames: Statistical Budgets and Mesh Quality Criterion,” *Combustion and Flame*, Vol. 157, No. 4, 2010, pp. 778–789.
<https://doi.org/10.1016/j.combustflame.2009.12.017>
- [33] Pope, S. B., *Turbulent Flows*, Cambridge Univ. Press, New York, 2000, pp. 575–578.
<https://doi.org/10.1017/CBO9780511840531>
- [34] Kempf, A., Flemming, F., and Janicka, J., “Investigation of Lengthscales, Scalar Dissipation, and Flame Orientation in a Piloted Diffusion Flame by LES,” *Proceedings of the Combustion Institute*, Vol. 30, No. 1, 2005, pp. 557–565.
<https://doi.org/10.1016/j.proci.2004.08.182>
- [35] Richardson, E. S., and Chen, J. H., “Application of PDF Mixing Models to Premixed Flames with Differential Diffusion,” *Combustion and Flame*, Vol. 159, No. 7, 2012, pp. 2398–2414.
<https://doi.org/10.1016/j.combustflame.2012.02.026>
- [36] Zhou, H., Li, S., Ren, Z., and Rowinski, D. H., “Investigation of Mixing Model Performance in Transported PDF Calculations of Turbulent Lean Premixed Jet Flames Through Lagrangian Statistics and Sensitivity Analysis,” *Combustion and Flame*, Vol. 181, July 2017, pp. 136–148.
<https://doi.org/10.1016/j.combustflame.2017.03.011>
- [37] Ren, Z., and Pope, S. B., “An Investigation of the Performance of Turbulent Mixing Models,” *Combustion and Flame*, Vol. 136, No. 1, 2004, pp. 208–216.
<https://doi.org/10.1016/j.combustflame.2003.09.014>
- [38] Cao, R. R., Wang, H., and Pope, S. B., “The Effect of Mixing Models in PDF Calculations of Piloted Jet Flames,” *Proceedings of the Combustion Institute*, Vol. 31, No. 1, 2007, pp. 1543–1550.
<https://doi.org/10.1016/j.proci.2006.08.052>
- [39] Krisman, A., Tang, J. C., Hawkes, E. R., Lignell, D. O., and Chen, J. H., “A DNS Evaluation of Mixing Models for Transported PDF Modelling of Turbulent Nonpremixed Flames,” *Combustion and Flame*, Vol. 161, No. 8, 2014, pp. 2085–2106.
<https://doi.org/10.1016/j.combustflame.2014.01.009>
- [40] Han, W., Raman, V., and Chen, Z., “LES/PDF Modeling of Autoignition in a Lifted Turbulent Flame: Analysis of Flame Sensitivity to Differential Diffusion and Scalar Mixing Time-Scale,” *Combustion and Flame*, Vol. 171, Sept. 2016, pp. 69–86.
<https://doi.org/10.1016/j.combustflame.2016.05.027>
- [41] Kuron, M., Hawkes, E. R., Ren, Z., Tang, J. C. K., Zhou, H., Chen, J. H., and Lu, T., “Performance of Transported PDF Mixing Models in a Turbulent Premixed Flame,” *Proceedings of the Combustion Institute*, Vol. 36, No. 2, 2017, pp. 1987–1995.
<https://doi.org/10.1016/j.proci.2016.05.019>
- [42] Wang, H., Pant, T., and Zhang, P., “LES/PDF Modeling of Turbulent Premixed Flames with Locally Enhanced Mixing by Reaction,” *Flow, Turbulence and Combustion*, Vol. 100, No. 3, 2017, pp. 1–29.
<https://doi.org/10.1007/s10494-017-9831-0>
- [43] You, J., Yang, Y., and Pope, S. B., “Effects of Molecular Transport in LES/PDF of Piloted Turbulent Dimethyl Ether/Air Jet Flames,” *Combustion and Flame*, Vol. 176, Feb. 2017, pp. 451–461.
<https://doi.org/10.1016/j.combustflame.2016.11.007>

- [44] Subramaniam, S., and Pope, S. B., "Comparison of Mixing Model Performance for Nonpremixed Turbulent Reactive Flow," *Combustion and Flame*, Vol. 117, No. 4, 1999, pp. 732–754.
[https://doi.org/10.1016/S0010-2180\(98\)00135-7](https://doi.org/10.1016/S0010-2180(98)00135-7)
- [45] Pope, S. B., "Small Scales, Many Species and the Manifold Challenges of Turbulent Combustion," *Proceedings of the Combustion Institute*, Vol. 34, No. 1, 2013, pp. 1–31.
<https://doi.org/10.1016/j.proci.2012.09.009>
- [46] Klimenko, A. Y., and Pope, S. B., "The Modeling of Turbulent Reactive Flows Based on Multiple Mapping Conditioning," *Physics of Fluids*, Vol. 15, No. 7, 2003, pp. 1907–1925.
<https://doi.org/10.1063/1.1575754>
- [47] Cleary, M., and Klimenko, A. Y., "A Generalised Multiple Mapping Conditioning Approach for Turbulent Combustion," *Flow, Turbulence and Combustion*, Vol. 82, No. 4, 2009, pp. 477–491.
<https://doi.org/10.1007/s10494-008-9161-3>
- [48] Pope, S. B., "A Model for Turbulent Mixing Based on Shadow-Position Conditioning," *Physics of Fluids*, Vol. 25, No. 11, 2013, Paper 110803.
<https://doi.org/10.1063/1.4818981>
- [49] Zhao, X., Bhagatwala, A., Chen, J. H., Haworth, D. C., and Pope, S. B., "An a Priori DNS Study of the Shadow-Position Mixing Model," *Combustion and Flame*, Vol. 165, March 2016, pp. 223–245.
<https://doi.org/10.1016/j.combustflame.2015.12.009>
- [50] Mantel, T., and Borghi, R., "A New Model of Premixed Wrinkled Flame Propagation Based on a Scalar Dissipation Equation," *Combustion and Flame*, Vol. 96, No. 4, 1994, pp. 443–457.
[https://doi.org/10.1016/0010-2180\(94\)90110-4](https://doi.org/10.1016/0010-2180(94)90110-4)
- [51] Swaminathan, N., and Bray, K., "Effect of Dilatation on Scalar Dissipation in Turbulent Premixed Flames," *Combustion and Flame*, Vol. 143, No. 4, 2005, pp. 549–565.
<https://doi.org/10.1016/j.combustflame.2005.08.020>
- [52] Kolla, H., Rogerson, J., Chakraborty, N., and Swaminathan, N., "Scalar Dissipation Rate Modeling and Its Validation," *Combustion Science and Technology*, Vol. 181, No. 3, 2009, pp. 518–535.
<https://doi.org/10.1080/00102200802612419>
- [53] Stöllinger, M., and Heinz, S., "Evaluation of Scalar Mixing and Time Scale Models in PDF Simulations of a Turbulent Premixed Flame," *Combustion and Flame*, Vol. 157, No. 9, 2010, pp. 1671–1685.
<https://doi.org/10.1016/J.COMBUSTFLAME.2010.01.015>
- [54] Kuron, M., Ren, Z., Hawkes, E. R., Zhou, H., Kolla, H., Chen, J. H., and Lu, T., "A Mixing Timescale Model for TPDF Simulations of Turbulent Premixed Flames," *Combustion and Flame*, Vol. 177, March 2017, pp. 171–183.
<https://doi.org/10.1016/j.combustflame.2016.12.011>

V. Raman
 Associate Editor